# Chapter 16
# Hemodynamic Aspects of Vessel Wall Imaging: 4D Flow

**Pim van Ooij and Michael Markl**

## Introduction

Cardiovascular MRI has undergone substantial developments over the last decades and offers capabilities for evaluating cardiac anatomy and function including the assessment of vascular anatomy and blood flow dynamic. Phase contrast (PC) MRI can be used to measure and quantify pulsatile blood flow in the human vascular system.

The basic principle has already been introduced by Carr and Purcell in 1954 who reported the observation of coherent motion on the MR signal [1] and by Hahn in 1960 who proposed to use nuclear precession to measure the velocity of sea water by means of phase shifts produced by magnetic field gradients [2]. Two decades later, Grant and Back were among the first to investigate the possibility of measuring flow velocity with MRI [3]. They called the technique "NMR rheotomography" and were visionary by remarking that "rheotomography may prove to be particularly useful for the noninvasive diagnosis of cardiovascular defects." Nearly 40 years later, many groups worldwide are using MRI flow measurements for the noninvasive diagnosis of cardiovascular defects. The first in vivo velocity map images and applications were reported in the early 1980s [4–7]. The initial measurement of a through-plane velocity profile in a two-dimensional (2D) slice of water flowing

P. van Ooij

Department of Radiology & Nuclear Medicine, Amsterdam University Medical Centers, location AMC, Amsterdam, The Netherlands

M. Markl (✉)

Department of Radiology, Northwestern University, Feinberg School of Medicine, Chicago, IL, USA

Department of Biomedical Engineering, McCormick School of Engineering, Northwestern University, Evanston, IL, USA

e-mail: mmarkl@northwestern.edu

through a glass U-tube has evolved, and 2D and time-resolved (ECG-gated "CINE" imaging) PC-MRI has become available on all modern MR systems and is an integral part of clinical protocols assessing blood flow in the heart and large vessels [8–10]. More recently, the combination of CINE PC-MRI with three-dimensional (3D) spatial encoding and three-directional velocity encoding (termed "4D flow MRI") has made possible measurements of 3D blood flow dynamics in a 3D volume and over time (4D = 3D + time) [11–13].

This chapter will review the journey from simple 2D to 4D flow MRI for the advanced quantification and visualization of hemodynamic measures in vessel wall disease. We will describe the fundamental concepts of 4D flow MRI in terms of acquisition, data processing, as well as its applications to the assessment of altered blood flow dynamics in vascular diseases. A special emphasis is on the potential of 4D flow MRI to quantify important characteristics of the vessel wall such as wall shear stress (WSS) or pulse wave velocity (PWV). The chapter will conclude with a discussion of the current role of 4D flow MRI and future directions.
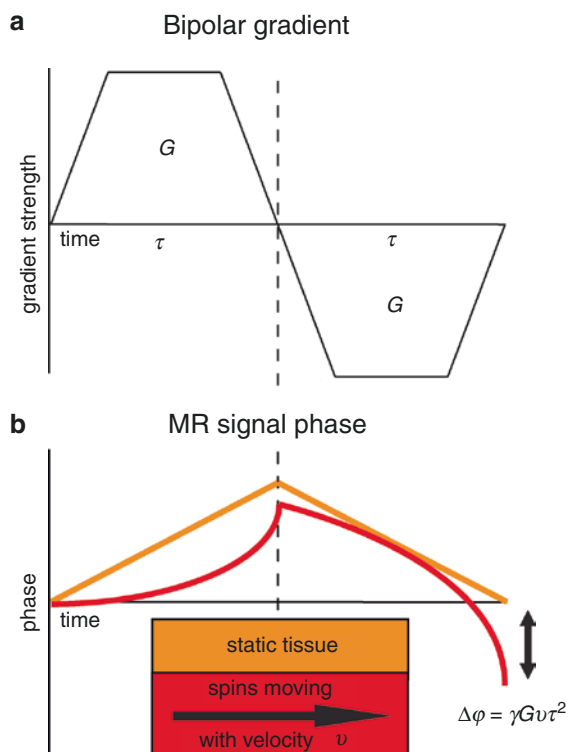
## Background

### *From 2D to 4D Flow Image Acquisition*

Flow imaging with MRI is based on the phase contrast (PC) technique, which enables the acquisition of spatially registered information on blood flow velocities simultaneously with morphological data within a single MRI measurement. In current clinical routine, PC-MRI is typically accomplished using methods that resolve two spatial dimensions (2D) in individual slices and encode a single time-resolved component of velocity directed perpendicularly to the 2D slice (through-plane velocity encoding). This approach allows measurements of forward, regurgitant, and shunt flows in congenital and acquired heart disease. In MRI, magnetic field gradient coils can create linearly varying magnetic fields along all three spatial dimensions on top of the main (static) magnetic field $B_0$. These magnetic field gradients cause spatially varying phase shifts of the source of the MRI signal (^{1}H proton spins in the human body) depending on the location of the source along the gradient. Spins that move along the direction of the gradient, e.g., flowing blood, acquire a different phase shift than the spins in adjacent static tissue [14].

The phase shift of the static media can be nulled by applying a magnetic field gradient with opposite polarity, whereas a phase shift for the moving spins will accumulate. The combination of both gradients is called a bipolar gradient [4] (see Fig. 16.1).

Using appropriate bipolar velocity encoding gradients, flow-dependent phase changes can be measured by playing out two acquisitions with different velocity dependent signal phase but otherwise identical sequence parameters. Subtraction of the two resulting phase images (i.e., calculation of phase difference images) allows

**Fig. 16.1** (**a**) A bipolar gradient that causes (**b**) a phase shift for moving spins compared to zero phase for static spins. The phase shift $\Delta\varphi$ is proportional to the gyromagnetic ratio $\gamma$, the gradient strength $G$, the velocity of the moving spins $v$, and the gradient duration $\tau$. Note that the equation represents a simplified situation where grant ramps are ignored for then coagulation of the calculation of phase shift $\Delta\varphi$



for the removal of the unknown background phase and calculation of velocity images [9].

With a bipolar gradient applied to the main direction of the blood flow, single-direction (e.g., through-plane) blood flow velocity is measured. Bipolar gradients can also be subsequently applied to two or three orthogonal axes to resolved blood flow velocities in two or three dimensions [15, 16].

To measure temporally resolved pulsatile blood flow velocities, a time-resolved (CINE) measurement can be performed [17, 18]. As illustrated in Fig. 16.2, PC-MRI data acquisition is split over multiple heartbeats, and data acquisition is gated to the cardiac cycle using the ECG signal (e.g., the R-wave) or a pulse oximeter reading. A series of time-resolved (CINE) images is collected representing the dynamics of the pulsatile blood flow during the cardiac cycle. Usually, one-directional ("through-plane") velocity encoding along the predominant blood flow direction is used to quantify blood flow in the heart, through cardiac valves, and in arteries and veins throughout the body. Typical 2D CINE PC-MRI images are illustrated in Fig. 16.2.

For over three decades, 2D CINE PC-MRI has been widely used for flow quantification in the aorta [19], the carotid arteries [20] and the intracranial vessels [21]. For routinely used 2D CINE PC-MRI, a slice for a 2D measurement is manually
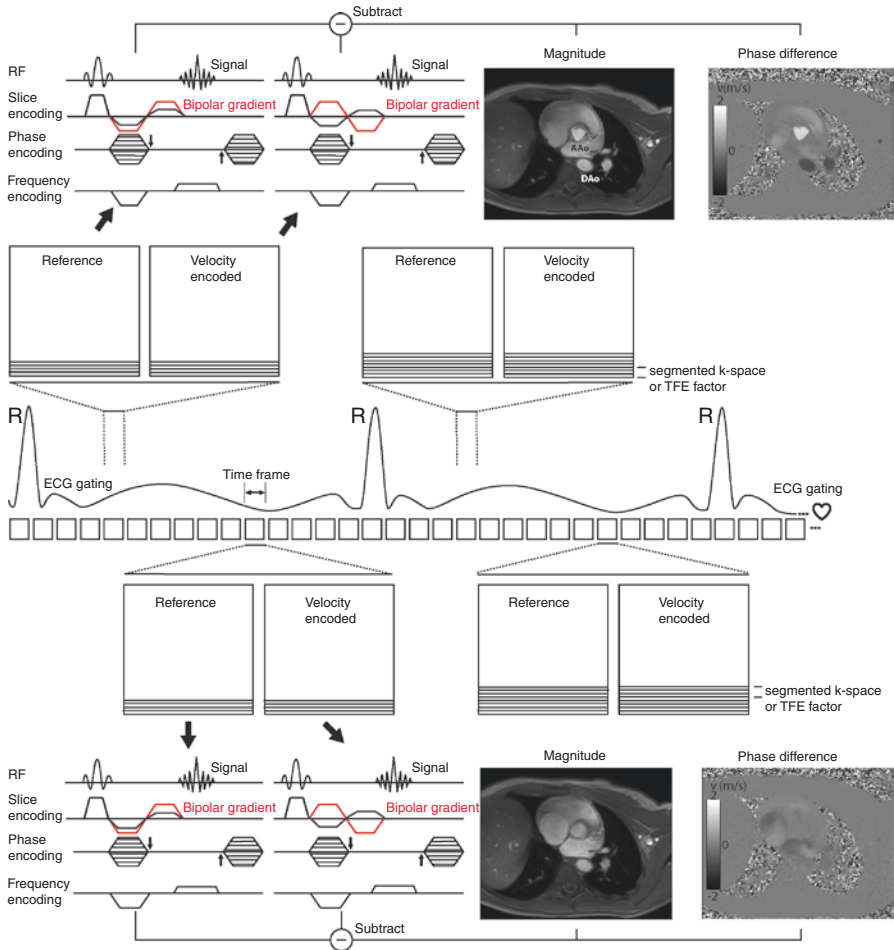
**Fig. 16.2** In 2D CINE PC-MRI, ECG triggering over multiple R-R intervals is used to acquire a series of time frames over the cardiac cycle. For each time frame, reference MRI raw data (k-space) lines (without bipolar gradient) and velocity encoded k-space lines (with bipolar gradient) are acquired. The number of k-space lines acquired for each time frame is determined by the segmented k-space or turbo field echo factor. After completion, phase contrast magnitude anatomical images and phase difference containing the velocity information are reconstructed. The figure illustrates 2D PC-MRI acquisition at the site of the aortic valve peak systole (top) and diastole (bottom)

positioned perpendicular to a vessel, and blood flow velocity is encoded in one direction through the 2D slice. However, placement of the acquisition plane remains challenging and can lead to the underestimation of peak velocities if misplaced or not orthogonal to the flow of interest. This is a common occurrence in cases involving complex flow and where changes in flow direction occur throughout the cardiac cycle, such as with valvular stenosis, valvular regurgitation, complex congenital

heart disease, or aneurysms. These challenges can be addressed by three-dimensional (3D) PC-MRI with three-directional velocity encoding which can provide comprehensive information on the in vivo 3D blood flow dynamics with full volumetric coverage of the vascular region of interest. Wigström et al. were the first to implement a high spatial resolution and electrocardiogram (ECG)-gated 3D cine phase contrast pulse sequence, currently known as 4D flow MRI (4D = 3D+ time over the cardiac cycle, flow = three-directional velocity encoding) [22].
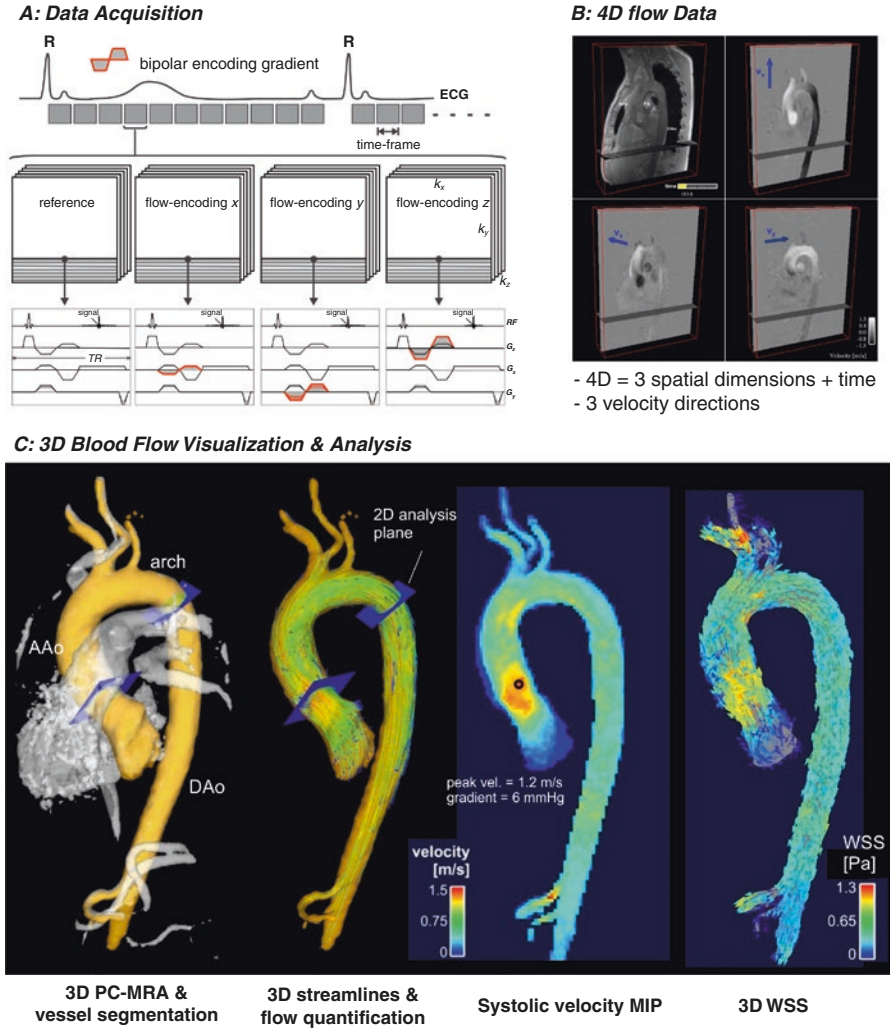
## 4D Flow Acquisition Methods and Techniques

### *Data Acquisition*

In 4D flow MRI, velocity is encoded along all three spatial dimensions throughout the cardiac cycle, thus providing a time-resolved 3D velocity field [8, 23, 24]. As shown in Fig. 16.3a, three-directional velocity measurements can be achieved by interleaved four-point velocity encoding which acquires one reference image and three velocity-encoded images along three orthogonal ($x$, $y$, $z$) directions [25–27]. As for 2D CINE PC-MRI, data acquisition is synchronized with the cardiac cycle, and data collection is distributed over multiple cardiac cycles using "k-space segmentation" techniques (only a fraction of the entire 4D flow data is measured during each cardiac cycle; the data is successively collected over multiple RR intervals). For prospective ECG gating, where the acquisition starts after receiving the R signal of the QRS complex, some dead time toward the next R-wave should be reserved to account for heartbeat variations. The late portion of diastole is therefore not measured [17]. With retrospective gating, continuous acquisition is not synchronized to the heartbeat. Each k-space line is time-stamped and retrospectively interpolated to fixed time frames in the cardiac cycle, thereby enabling acquisition of the diastolic phases. After completion of the 4D flow acquisition, four time-resolved (CINE) 3D data sets are generated ("magnitude" data depicting anatomy and three flow data sets representing velocities "$V_x$, $V_y$, and $V_z$") as illustrated in Fig. 16.3b.

It should be noted that increasing 4D flow spatial resolution by reducing voxel size is possible but is accompanied by a decrease in signal-to-noise ratio (SNR) and thus image quality. Moreover, for volumetric acquisitions such as 4D flow MRI, scan times increase cubically with isotropic voxel size reduction.

An important (user-defined) 4D flow MRI parameter is the velocity encoding sensitivity (VENC), which represents the maximum flow velocity that can be acquired without velocity aliasing. When a velocity in a voxel exceeds VENC, velocity aliasing can occur which is typically visible as a sudden change from high to low velocity within a region of flow (see Fig. 16.4). If aliasing artifacts are present, accurate flow visualization and quantification may be compromised unless anti-aliasing correction can be successfully performed [28]. It is important to note, however, that velocity noise is directly related to the VENC [8]. Therefore, selecting a high VENC may alleviate the issue of velocity aliasing but will also increase the

**A: Data Acquisition**



**B: 4D flow Data**



- 4D = 3 spatial dimensions + time
- 3 velocity directions

**C: 3D Blood Flow Visualization & Analysis**



| 3D PC-MRA & vessel segmentation | 3D streamlines & flow quantification | Systolic velocity MIP | 3D WSS |

**Fig. 16.3** Acquisition of 4D flow MRI data and analysis of hemodynamic metrics in the thoracic aorta of a healthy subject. (**a**) ECG synchronized 4D Flow MRI data acquisition. For each time frame, four 3D raw data sets are collected to measure three-directional blood flow velocities ($v_x$, $v_y$, $v_z$) with a reference scan and three velocity encoded acquisitions. k-space segmentation is used to collect a subset ($N_{Seg}$) of all required raw data (k-space) lines for each time frame. The selection of $N_{Seg}$ determines the temporal resolution and total scan time. (**b**) 4D flow data comprises information along all three spatial dimensions, three velocity directions, and time in the cardiac cycle. (**c**) A 3D phase contrast angiogram (3D PC-MRA) can be calculated from 4D flow MRI data to aid visualization and provide a basis for the 3D segmentation of the aorta (orange rendering of aorta). Systolic streamlines allow for visual assessment of flow patterns and placement of analysis planes for retrospective flow quantification. Calculation of a systolic velocity maximum intensity projections (MIP) provides an overview over systolic velocity distribution and allows for volumetric quantification of peak systolic velocity (location of peak velocity is indicated by black circle in the ascending aorta). Advanced vessel wall characteristics can be derived such as systolic 3D wall shear stress (WSS) vectors along the aorta. AAo ascending aorta, DAo descending aorta
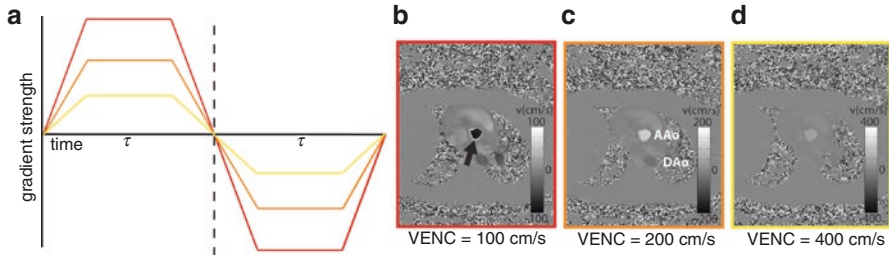
**Fig. 16.4** (**a**) Bipolar gradients of higher strength and thus a low-VENC cause (**b**) aliasing (black arrow) in the phase difference images of the aorta, whereas aliasing is avoided when VENC is tailored to the expected maximum velocity in (**c**). (**d**) At a high VENC, the sensitivity to changes in aortic velocities is decreased. AAo ascending aorta, DAo descending aorta

**Table 16.1** Typical (ranges of) scan parameters for three different anatomical regions

|  | k-space segmentation (turbo field echo factor) | (Isotropic) spatial resolution (mm³) | Temporal resolution (ms) | VENC (cm/s) |
|---|---|---|---|---|
| Heart/aorta | 1–3 | 2.0–3.0 | 20–60 | 150–400 |
| Carotid | 2–3 | 0.8–1.4 | 40–60 | 100–150 |
| Intracranial | 2–4 | 0.5–1.2 | 40–80 | 70–150 |

level of velocity noise in flow velocity images. VENC should thus be chosen as close to the peak velocity as possible. This is often accomplished by performing a fast low-resolution 2D PC-MRI "VENC scout" scan prior to 4D flow MRI to estimate the highest velocity in the vessel of interest and adjust VENC accordingly.

In Fig. 16.4, the principle of VENC is shown for through-plane 2D phase difference images of the aorta with severe velocity aliasing when the VENC is selected too low (high bipolar gradient). Unaliased flow velocities are achieved when the VENC is tailored to the expected maximum velocity (lower bipolar gradient).

In Table 16.1 typical ranges of scan parameters are shown for heart/aorta, carotid, and intracranial 4D flow MRI applications.

## Data Acquisitions: Imaging Acceleration Techniques

Long scan times on the order of 10–20 minutes have previously relegated 4D flower MRI to the realm of research. However, current implementations are quickly approaching clinically feasible scan times, on the order of 2–8 minutes. Methodological improvements include echo planar imaging (EPI), where multiple Cartesian readouts are acquired after one excitation to obtain high spatial resolution [29]. Additional imaging acceptation is based on parole imaging such as sensitivity encoding (SENSE) [30, 31], generalized autocalibrating partially parallel acquisitions (GRAPPA) [32], k-t acquisition speed-up techniques (k-t BLAST) [33, 34], k-t GRAPPA [35], k-t principal component analysis (k-t PCA) [36, 37], and

CIRCUS [38]. Another promising technique to accelerate 4D flow MRI is compressed sensing where data is acquired in a sparse and random manner followed by nonlinear recovery of data [39, 40]. For example, aortic 4D flow MRI is now possible with a scan time of less than 2 minutes without substantial degradation of image quality [41].

## *Data Acquisitions: Non-Cartesian Sampling*

An alternative technique that is increasingly used to accelerate 4D flow MRI is radial data sampling combined with undersampling (e.g., PC-VIPR – vastly undersampled isotropic projection reconstruction [42]). Radial sampling has two important advantages over Cartesian readouts: (1) sparse sampling results in streak image instead of fold-over artifacts which allows for higher undersampling factors [42] and (2) the center of k-space is continuously sampled and results in insensitivity to subject motion [43]. As an alternative, spiral k-space sampling can cover the entire k-space uniformly and rapidly [44], allowing for rapid 4D flow MRI velocity measurements [45–47]. However, both radial and spiral sampling are sensitive to eddy current effects which require efficient correction strategies, and image reconstruction is more computationally demanding. Alternatively, radial- and spiral-like trajectories can be implemented on a Cartesian grid, called pseudo-radial and pseudo-spiral trajectories [48, 49]. For example, a recently reported combination of pseudo-Cartesian acquisition schemes coupled with compressed sensing for imaging acceleration has shown great potential for fast and robust pediatric 4D flow MRI [50].

## *Data Acquisitions: Respiratory Control (Gating, Self-Gating)*

For cardiothoracic and abdominal applications, methods for respiration control are needed to prevent image deterioration due to respiratory motion. Early efforts in MRI have focused on gating of the respiratory signal using bellows [51] or navigator echoes in a longitudinal beam placed on the diaphragm [52]. Most methods are based on accepting data in the expiration phase when chest motion is minimal and rejecting data acquired in the inspiration phase when the chest is moving. Other strategies minimize respiration-related image degradation by respiratory ordered phase encoding (ROPE): measurements at inspiration are attributed to the center of k-space, whereas the measurements at expiration are attributed to the edges of k-space [53]. Such strategies have been successfully implemented for 4D flow MRI [54] in combination with navigator gating [55]. Other promising approaches employ self-gating techniques, e.g., cross-correlation with reference breathing motion to identify different respiratory phases [56] or extracting respiratory and cardiac motion signals from additional and repeatedly sampled central k-space data [57].

# 4D Flow Analysis Methods and Techniques

## *Preprocessing and Phase Offset Error Corrections*

4D flow MRI data are affected by systematic velocity encoding errors caused by magnetic field inhomogeneity, concomitant magnetic fields (Maxwell terms) [58], and eddy currents [59, 60]. Correction of these errors typically includes the identification of image regions that contain static tissue in order to estimate the spatial distribution of background phase offsets (using a first- or second-order fit to the static tissue phase difference data) [61]. Background phase errors can subsequently be removed by subtraction of the estimated offset from the entire velocity data [62].

It is common in 4D flow MRI that the VENC setting is lower than the maximum velocity in the measurement and that velocity aliasing occurs. With the assumption that adjacent pixel velocities in the temporal or slice direction should not differ more than VENC [28], aliased velocities can be automatically detected and corrected [63].

## *Visualization and Quantification of 4D Flow MRI Hemodynamics*

For effective visualization of the information encoded in the large 4D flow MRI data sets (see Fig. 16.3b), many methods have been developed and include velocity vector display in three-dimensional space [64, 65] streamlines [66, 67], and path lines/particle traces [67].

Figure 16.3c illustrates 4D flow MRI-based evaluation of fundamental (flow, peak velocity) and advanced hemodynamic metrics (wall shear stress, WSS) based on a single acquisition. Visualization of the vascular geometry can be achieved from a 4D flow acquisition by generating a non-contrast 3D PC-MR angiogram (MRA). A surface rendering of the vascular structure of interest (see Fig. 16.3c, left) allows for regional orientation, analysis, and flow visualization. For qualitative visualization of 4D flow MRI data, 3D streamlines or time-resolved 3D path lines can be used for flow pattern visualization. Streamlines represent the instantaneous blood flow vector field for a single cardiac time-frame. For example, Fig. 16.3c illustrates the use of systolic 3D streamlines to visualize the spatial distribution and orientation of blood flow velocities. Color-coding by velocity magnitude facilitates the visual identification of regions with high systolic flow velocities. For visualization of the temporal evolution of 3D blood flow, time-resolved path lines are the method of choice. Time-resolved path lines are best viewed and displayed dynamically (movie mode) to fully appreciate the dynamic information and changes in blood flow over the cardiac cycle. It is important to differentiate between streamlines and path lines since the former represents the instantaneous tangent to the velocity vector at a given time in the cardiac cycle (e.g., peak systole), while the latter resemble traces of the dynamically time-varying blood flow over the cardiac cycle. 4D flow MRI can also be used to derive volumetric and maximum intensity projections (MIPs) of
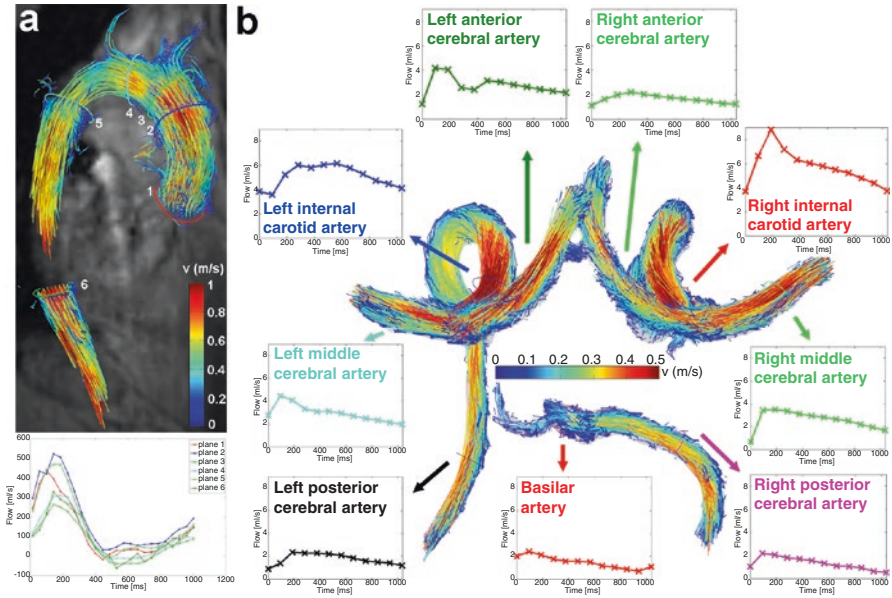
**Fig. 16.5** (**a**) 3D flow visualization (path lines and with flow quantification in perpendicular 2D analysis planes at standardized locations in the healthy aorta) [68]. (**b**) 3D segmentation and flow visualization in the circle of Willis of a healthy volunteer. Flow quantification based on perpendicular 2D analysis planes allows for the systematic assessment of blood flow over the cardiac cycle in the entire circle of Willis

peak velocity for easy volumetric identification of peak flow velocities (see Fig. 16.3c).

For quantification of flow in a vessel, 2D analysis planes can be placed at any location along the vessel of interest (Fig. 16.3c) to calculate peak and mean velocities, total flow, net flow, or retrograde flow. Figure 16.5a illustrates aortic 4D flow MRI with subsequent 3D flow visualization (path lines) and flow quantification in six 2D analysis planes distributed along the thoracic aorta. Figure 16.5b depicts an example of comprehensive cerebrovascular 4D flow with 3D blood flow visualization in the large intracranial arteries and quantification of flow-time curves at all major circle of Willis arteries.

## *Advanced Hemodynamic Vessel Wall Metrics*

In addition to 3D blood flow visualization and planar flow quantification, 4D flow MRI offers the opportunity to derive advanced hemodynamic measures such as vorticity [69, 70] and helicity [71, 72], wall shear stress (WSS) [73, 74],

pressure gradients [75, 76], viscous energy loss [77, 78], turbulent kinetic energy [79, 80], or pulse wave velocity (PWV) [81, 82]. This article will focus on the two parameters most relevant for vascular wall characterization: PWV and WSS.

**Pulse Wave Velocity**

It is well understood that arterial vascular stiffening (i.e., reduction of vessel wall elasticity) can lead to atherosclerosis and the development of vessel wall abnormalities and atherosclerotic plaques. Pulse wave velocity (PWV), the best known surrogate measure for arterial stiffness, is the speed of the pulsatile pressure wave that propagates along arteries in a heartbeat [83–85]. PWV is determined by the elastic modulus of the vessel, the vessel wall thickness, the vessel radius, and the density of blood (Moens-Korteweg equation) [85]. Thus, increased PWV is directly associated increased elastic modulus (i.e., stiffening) and vessel wall thickness. Both processes occur in early atherosclerosis, and PWV is thus considered an important indicator for the onset of this disease. A meta-analysis revealed that increased PWV and thus reduced aortic compliance is a strong predictor of future cardiovascular events and all-cause mortality. Moreover, an increase in aortic PWV by 1 m/s corresponded to an age-, sex-, and risk factor-adjusted risk increase of ca. 15% in total cardiovascular events [86]. Reliable measurement of PWV is thus of high interest, e.g., for monitoring vessel compliance during therapy [87, 88].

Carotid-femoral PWV using tonometry is the current reference standard to measure aortic compliance [89]. This method, however, is prone to errors and does not focus on regional compliance. Time-resolved 2D CINE PC-MRI provides a noninvasive estimate of PWV based on flow waveform measurements in analysis planes and allows focusing on the region of interest in patients, e.g., the thoracic aorta or carotid arteries [90–92]. Transit-time (TT) methods are typically employed to calculate temporal differences of specific flow waveforms features, e.g., timing differences of the foot of the waveform between two locations with known distance, as first described in 1989 for the aortic arch [93]. The accuracy of PWV quantification can be improved by adding velocity encoding directions [81] or using multiple measurement locations [94, 95].

PWV can be retrospectively quantified from 4D flow MRI data based on multiple pulsatile flow waveforms distributed homogenously along the entire course of the vessel. As shown in Fig. 16.6 for 4D flow-based PWV estimation in the thoracic aorta, flow-time curves are automatically extracted for each analysis plane, and a measure of blood travel time (e.g., time-to-foot) is derived. Aortic PWV (in m/s) is determined by a linear fit from data of the entire aorta [82, 96]. However, reliable PWV assessment requires measure of the rapid changes of which can only be achieved with sufficient temporal resolution.
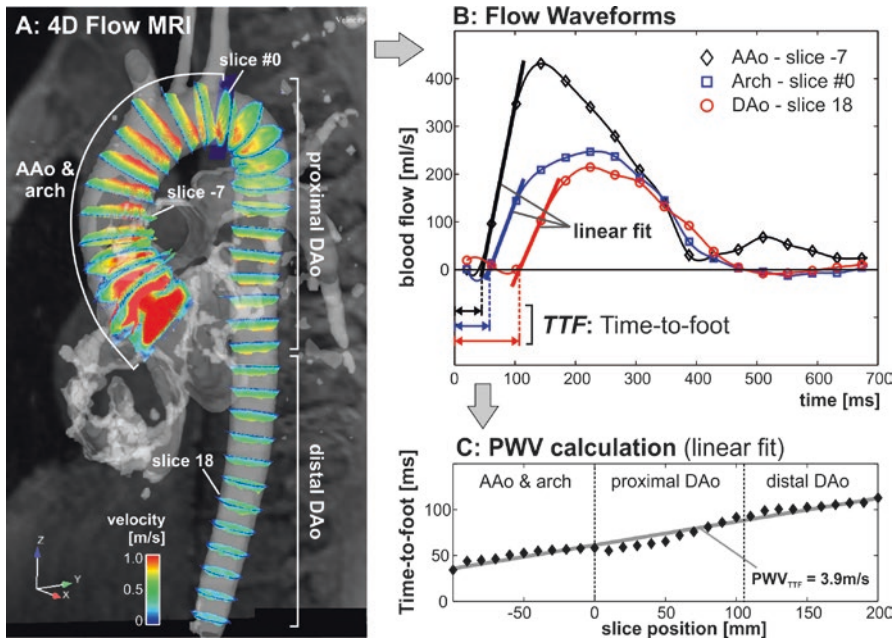
**Fig. 16.6** Derivation of aortic pulse wave velocity from 4D flow MRI: (**a**) flow curves are automatically extracted in multiple planes along the aortic centerline. An initial plane #0 is positioned at the proximal asking aorta. Subsequently, all other 2D analysis planes will be positioned downstream in fixed intervals. (**b**) For each analysis plane, flow-time curves are calculated and the time-delay between adjacent planes is derived. (**c**) Aortic PWV (in m/s) is determined by a linear fit from data of the entire aorta. AAo: ascending aorta, DAo: descending aorta

## Wall Shear Stress

The three-directional velocity fields can be used to calculate WSS (i.e., the blood shear rate on the endothelial cells that line the vessel wall multiplied by blood viscosity), a known pathophysiological stimulus cited to alter gene expression and endothelial cell function [97]. Altered shear forces at the intimal surface can promote endothelial changes and create areas at risk for vascular remodeling, i.e., when high WSS is sensitized, growth factors and other molecules such as nitric oxide (NO) and matrix metalloproteinases (MMPs) are released to dilate the vessel to restore the normal WSS value [98]. Altered WSS has been associated with the development of vulnerable plaques in the carotid arteries [99], progressive aortic dilation [100, 101], or development of cerebrovascular aneurysms [102–104]. WSS can be estimated from 4D flow MRI data by multiplying the deformation tensor $\dot{\varepsilon}$ that contains the velocity gradients in all directions at the wall, with the viscosity of blood. As schematically illustrated in Fig. 16.7 (top), initial studies have employed 4D flow MRI to quantify regional time-resolved WSS based on 2D analysis planes [105]. The variation of WSS direction over the cardiac cycle can be used to calculate the oscillatory shear index (OSI) [106]. More recently, methods have been

## 1. Time-resolved 3D segmental WSS on 2D plane
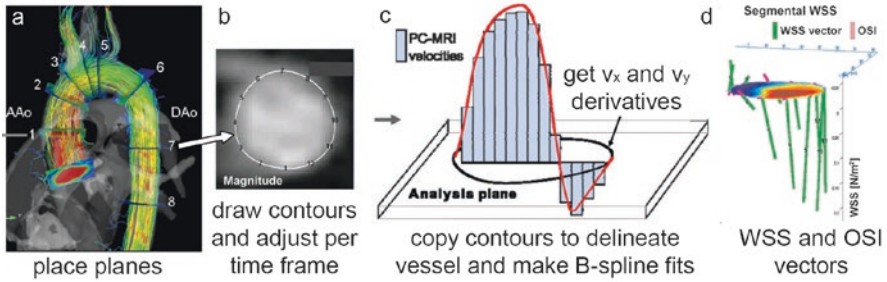


## 2. 3D WSS on entire geometry (systole only)
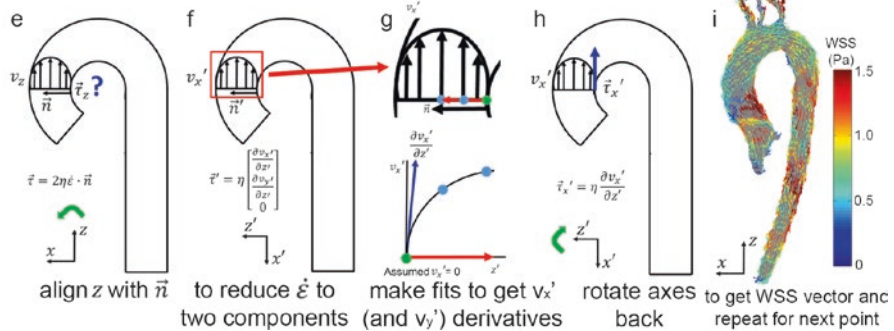


**Fig. 16.7** (1) 3D segmental WSS in 2D planes. (**a**) Planes are placed perpendicularly to the aorta measured with 4D flow MRI, (**b**) contours are manually drawn to delineate the vessel wall and to define the segments for WSS calculation, (**c**) B-spline fits through the $v_x$ and $v_y$ velocities are created to derive the gradients at the wall that after multiplication with blood viscosity, (**d**) yield the WSS vectors in the plane. When repeated for all time frames, OSI can be calculated. (2) 3D WSS on the entire aorta surface. (**e**) At each point along the vessel wall, the $z$-axis is aligned with the inward normal vector, and with the assumption that there is no velocity through the wall, the deformation tensor is reduced from nine components to two (**f**). Spline fits along the $x$ and $y$ velocities along the normal vector yield the $v_x$ and $v_y$ derivatives. After multiplication with viscosity and rotation back to the original axes system, the local WSS vector is obtained

developed to compute volumetric 3D WSS along the 3D surface of the entire aorta, carotid or intracranial vasculature, or aneurysms (Fig. 16.7, bottom) [74, 107–109]. For the aorta, a method for the quantification of turbulent WSS variation was recently developed [110].

Although 3D WSS mapping allows for compact visualization of hemodynamic parameters (see Fig. 16.7, (2)), it does not detect where "abnormal" values are present. In addition, aortic WSS undergoes significant changes during healthy aging which underlines the importance of age-matched control cohorts in clinical studies to identify patients with altered WSS [111]. To address this limitation, a "WSS heatmap concept" was recently developed which offers the opportunity to quantify the extent of altered WSS [112]. The method is based on aortic 4D flow MRI data of a healthy control population to create an aortic "WSS atlas." As shown in Fig. 16.8, the aortic
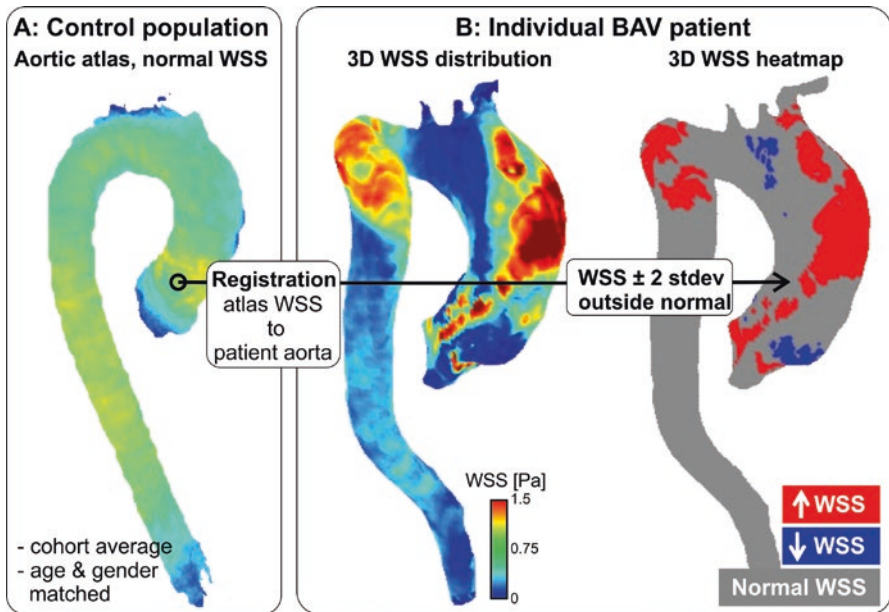
**Fig. 16.8** Patient-specific WSS heatmaps. (**a**) A 3D cohort-averaged WSS map of a control cohort ("WSS atlas") is used as reference to provide mean, median, and normal confidence intervals (CI = ± 2 standard deviations, SD) of the normal physiologic aortic WSS distribution. (**b**) After delineating the regions of abnormal WSS for an individual patient, defined as values outside the CI, heatmaps of abnormally elevated or decreased WSS are created

atlas establishes regional confidence intervals for normal physiologic WSS throughout the aorta. Patient-specific WSS is then co-registered to the healthy control atlas to calculate heatmaps which represent regions of abnormally low or high WSS (i.e., outside of the 95% confidence interval provided by the control WSS atlas).

It should be noted that the discrete nature of the 4D flow MRI measured velocity field will result in a systematic underestimation of WSS. This is a common limitation of the technique. While absolute accuracy when assessing WSS in vivo is challenging, the relative pattern of expression (and magnitude) can reliably be inferred, especially if scan parameters and the procedure for WSS estimation are consistent between study populations [113, 114].

# 4D Flow MRI in Vessel Wall Disease: From Head to Toe

## *Head*

In clinical practice, transcranial Doppler ultrasound is routinely used for cerebrovascular flow measurements. However, the technique is operator-dependent and limited by the acoustic windows of the head. 2D PC-MRI can provide reliable flow

measurements in large intracranial arteries and veins, not limited by location. However, challenges for using 2D PC-MRI for flow measurement include small and tortuous vessels [115], complex vascular anatomy, and need for the manual placement of 2D imaging planes in multiple vessel segments. As an alternative, 4D flow MRI is increasingly used to assess cerebrovascular 3D blood flow [116, 117]. Emerging applications include the hemodynamic evaluation of intracranial aneurysms, arteriovenous malformations (AVM), and intracranial atherosclerotic disease (ICAD). Several groups have reported the successful measurement and evaluation of flow and WSS in intracranial aneurysms in patient feasibility studies [107, 118–121], indicating the potential of flow MRI to assist in the classification of individual aneurysms pre-intervention.

**Arteriovenous Malformations (AVMs)**

In patients with cerebral AVMs, flow information is potentially valuable for a better understanding of the impact of a focal AVM on the flow redistribution in the brain and/or in treatment planning by attempting to identify the feeding arteries with highest flow (see Fig. 16.9), enabling efficient and targeted embolization treatment. Recent reports include the quantification of flow and WSS in patients using a highly optimized radial 4D flow technique [108, 122]. Additional studies demonstrated the potential of 4D flow MRI for the evaluation of global and regional AVM flow
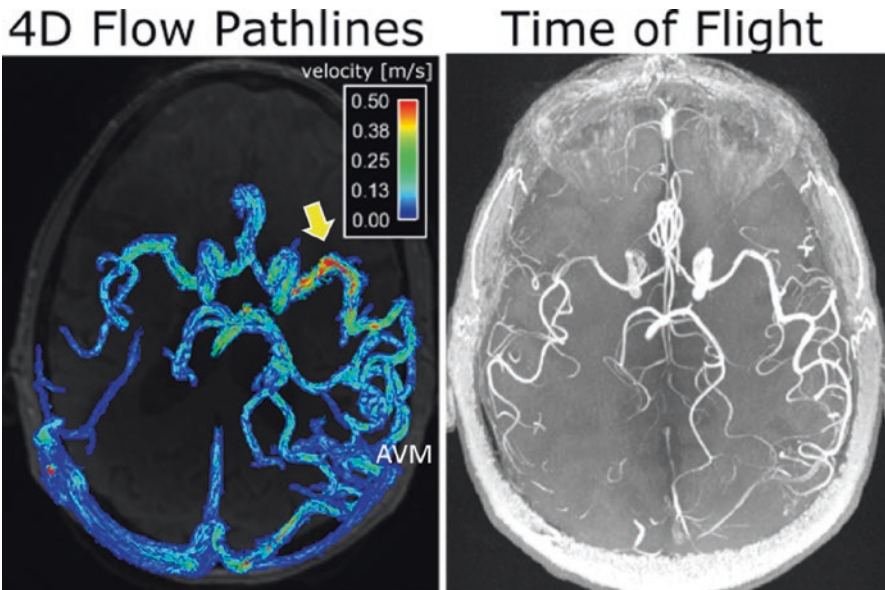


**Fig. 16.9** Intracranial 4D flow MRI (left) and time-of-flight (TOF) 3D angiogram (right) in a 62-year-old male patient with a large cerebral AVM (Spetzler-Martin grade = 3). The dense AVM vascular network and high flow velocity in a main AVM feeding artery (arrow) can clearly be appreciated

characteristics [123, 124]. The findings showed that 4D flow MRI can assess treatment-induced changes in cerebrovascular flow distribution and was able to demonstrate significant associations between 4D flow metrics, cerebral perfusion indices, and AVM risk factors such as the Spetzler-Martin grade [124].

**Intracranial Atherosclerotic Disease (ICAD)**

Intracranial atherosclerotic plaques can alter local and global hemodynamics (particularly proximal or distal to stenosed vessels). Currently, intracranial hemodynamic disturbance in patients with ICAD is primarily assessed using transcranial Doppler ultrasound. Few studies have been performed to characterize the 3D blood flow disturbance and flow redistribution across the major cerebral arteries in patients with ICAD. An early study by Hope et al. reported that TOF MRA overestimated the degree of stenosis and that 4D flow MRI velocity measurements could improve accuracy of diagnosis, when compared to catheter angiography [119]. It should be noted that current flow imaging techniques (2D and 4D) are limited by insufficient spatial resolution for the characterization of blood flow at sites of critical or severe stenosis. Instead, post-stenotic flow is typically used to represent the regional flow in the stenotic artery. Higher magnetic field (7 Tesla) with increased spatial resolution may be required for improved flow assessment in the smaller vessels [125].

**Intracranial Aneurysm**

A large number of studies investigating flow patterns in intracranial aneurysms were based on computational fluid dynamics (CFD) techniques in conjunction with subject-specific geometries extracted from medical images [126–129]. Findings from these studies revealed a wide variety of complex intra-aneurysmal flow patterns that were strongly dependent on patient-specific vascular geometry. In addition, a number of studies showed that changes in WSS along the wall of intracranial aneurysms may be associated with risk of aneurysm growths or rupture [73, 107, 121]. However, CFD has limitations such as assumptions concerning blood properties, boundary conditions, and vessel properties [129–131]. As an alternative, 4D flow MRI is increasingly used to assess intra-aneurysmal 3D hemodynamics in vivo. Several groups have reported the successful measurement and evaluation of intra-aneurysmal flow and WSS in patient feasibility studies [73, 116, 119, 132–137], indicating the potential of flow MRI to assist in the classification of individual aneurysms pre-intervention.

## *Neck*

Carotid artery stenosis is a leading cause of ischemic stroke, and detailed insights into the causes for the development of atherosclerosis at this site are of interest. Among other risk factors, it is assumed that the development of atherosclerosis in

the naturally bulbic ICA is related to local hemodynamic conditions such as flow deceleration or recirculation associated with reduced and oscillating WSS [138]. Particularly, low absolute WSS and high OSI are hypothesized to determine the composition of atherosclerotic lesions and the development of high-risk plaques [99, 102]. Since blood flow through the carotid bifurcation is complex with non-symmetric flow profiles, the full three-directional velocity information by 4D flow MRI can be useful for a complete in vivo assessment of the segmental distribution of WSS.

4D flow studies analyzing WSS in the normal carotid bifurcation confirmed that potentially atherogenic wall (e.g., low WSS) parameters were predominantly concentrated at the posterior wall of the proximal ICA [139, 140]. Cibis et al. found lower WSS in regions of higher wall thickness in the carotid bifurcation [141, 142]. An example of a cohort-averaged map showing low WSS at locations of high wall thickness is displayed in Fig. 16.10. The wall thickness map is in concordance with the tendency of carotid atherosclerosis to affect the outer walls of arterial bifurcations and to mostly develop in the proximal part of the ICA bulb [143, 144]. Moreover, a significant relationship between the size of regions exposed to altered wall parameters and the individual bifurcation geometry was demonstrated, similar to carotid bifurcation study using CFD [138]. In patients with ICA stenosis, markedly altered filling and helix formation in the ICA bulb were observed, while revascularization partly restored normal filling and helix formation [145]. Furthermore, a direct comparison of mean and absolute flow velocities in the common carotid artery (CCA) between 4D flow MRI and Doppler ultrasound showed good agreement despite general underestimation of peak velocities by MRI [146].

4D flow MRI-derived WSS quantification could thus be a valuable technique to assess the individual risk of flow-mediated atherosclerosis and carotid plaque progression.
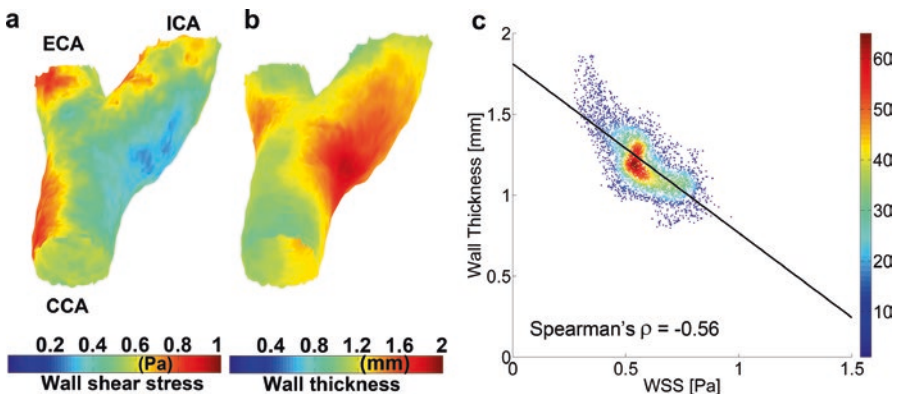


**Fig. 16.10** Three-dimensional (**a**) wall shear stress and (**b**) wall thickness carotid bifurcation maps averaged over 20 subjects with plaques. In (**c**) the correlation between WSS and WT is shown with color-coding for the density of the points

The assessment of PWV in the carotid arteries as a measure of vessel stiffness (and thus atherosclerotic burden) is challenging due its small size that necessitates high spatial and temporal resolution [147]. It is thus challenging to derive PWV using 4D flow MRI in the carotid arteries. For the determination of local PWV in the carotid arteries, the temporal resolution of through-plane 2D CINE PC-MRI was recently drastically improved by compressed sensing acceleration [148]. These novel acquisition strategies hold promise for future applications of either 2D or 4D flow MRI-derived PWV.

## *Thorax*

Cardiothoracic 4D flow imaging is typically performed as part of a standard-of-care aortic/pulmonary imaging protocol, which includes additional MRI techniques for the assessment of cardiac function and wall motion (CINE imaging), aortic and pulmonary dimensions and geometry (MR angiography), as well as aortic and pulmonary valve morphology and dynamics (CINE imaging). The combination with 4D flow MRI provides a comprehensive assessment of aortic/pulmonary structure and function. These data have contributed to the understanding of the development of vessel wall abnormalities (atherosclerosis, aortic dilation, aneurysm) as a consequence of thoracic vascular diseases such as aortic valve diseases (stenosis, insufficiency, congenital bicuspid aortic valve (BAV)), aortic coarctation, or Marfan syndrome.

**Aortic Valve Disease and Aortopathy**

The presence of aortic valve disease significantly alters the hemodynamic environment in the thoracic aorta. Several studies have shown promise of 4D flow MRI-based blood flow visualization for the investigation of valve-related abnormal flow patterns (e.g., aberrant vortex or helix flow) as shown in Fig. 16.11. However, the visual evaluation of changes in aortic flow patterns (e.g., grading of vortex of helix flow) can be limited by lack of standardization, observer bias, and thus reproducibility. A more effective and representative assessment is provided by the calculation of 4D flow-derived measures that quantify the impact of altered flow characteristics on the vessel wall, such as flow displacement and WSS.

Flow displacement is an easy to obtain quantitative marker that represents outflow asymmetry (i.e., deviation for a symmetric flow profile). Studies have shown that flow displacement can detect altered systolic outflow patterns in patients with different types and severity of aortic valve disease [149–153] or in patients with aortic dilation [154]. For example, recent studies showed that different aortic valve fusion phenotypes in patients with BAV resulted in distinctly altered eccentric aortic outflow jet patterns [101, 155]. Differences in aortic dilation type were associated
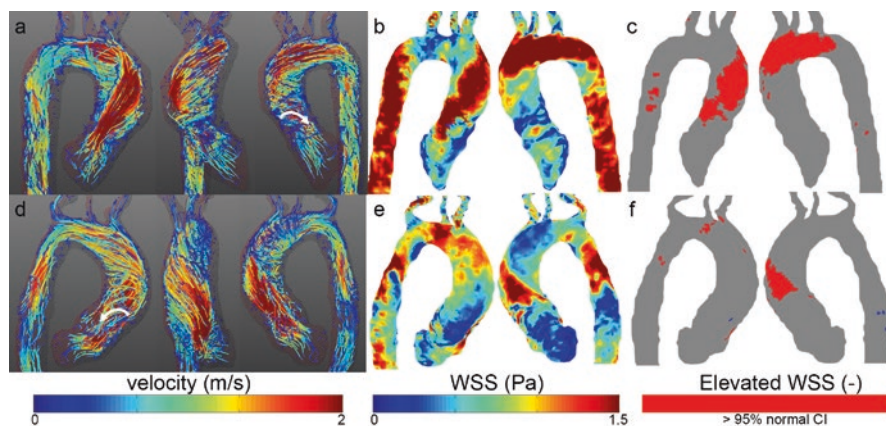
**Fig. 16.11** Velocity and WSS in two patients with a stenosed bicuspid aortic valve. (**a**, **d**) Peak systolic velocity path lines showing right-handed helical flow (top) and left-handed helical flow (bottom). Vortex flow can be seen as well (white arrows). (**b**, **e**) Stenotic flow leads to high wall shear stress on the right-anterior aortic wall (top) and left-posterior wall (bottom) which can be concisely visualized by elevated WSS heatmaps (**c**, **f**)

with altered flow displacement in the ascending aorta, suggesting a physiologic mechanism by which valve morphology can influence aortic wall remodeling.

Patient studies have demonstrated the potential of WSS to quantify the impact of deranged flow on the aortic wall. Initial 4D flow studies were based on 2D-based planar quantification of WSS changes in patients with aortic dilation [156], aortic atherosclerosis [157], or aortic valve abnormalities such BAV disease [101, 158–160]. Bieging et al. were the first to create a 3D segmentation of the aorta for the purpose of regional WSS estimation in patients with ascending aortic aneurysms [74]. More recently, Potters et al. used a modified algorithm to estimate 3D WSS on the entire aorta surface [109].

Interestingly, several 4D flow MRI studies have shown that the presence of aortic valve disease has a very different effect on aortic hemodynamics as compared to aortic dilation or aneurysm alone. Aortic dilation with an otherwise normal aortic valve generally leads to slow helix-type flow with significantly reduced WSS in the ascending aorta. In contrast, BAV or aortic valve stenosis will result in significantly elevated flow velocities, high-velocity transvalvular outflow jets, and eccentrically elevated WSS. These findings have been confirmed by a series of studies by Bissel et al., Mahadevia et al., Shan et al., and Rodríguez-Palomares et al. in larger cohorts (65–142 subjects, respectively) [100, 101, 155, 161]. A recent large cohort 4D flow MRI study in patients with aortic valve disease (>500 subjects) confirmed these findings. As shown in Fig. 16.12, aortic 4D flow MRI can be used to show the incidence of elevated WSS for specific groups of patients and healthy controls. Results clearly showed that aortic valve stenosis resulted in a marked increase in regional WSS compared to patients with aortic dilation but normal tricuspid aortic valve
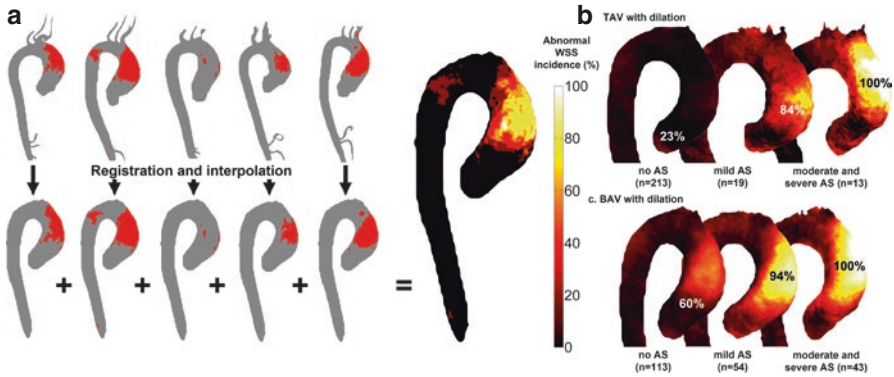
**Fig. 16.12** (**a**) Registration and interpolation techniques are used to project regions of elevated WSS onto a shared aortic geometry. Summing elevated WSS regions yields a map of the regional incidence of elevated WSS. Group-specific 3D maps of abnormally elevated WSS for (**b**) tricuspid aortic valve (TAV) with dilation with no aortic valve stenosis (AS), mild AS and moderate and severe AS, and (**c**) BAV patients with right non-valve function morphology (RN-BAV) with no AS, mild AS, and moderate and severe AS

[162]. In addition, the WSS heatmap concept can be employed to highlight regions with abnormally elevated WSS in individual patients (see Fig. 16.12) [163].

A recent study utilized the WSS heatmap concept to assess the correlation between abnormal in vivo 3D WSS and regional aortic tissue remodeling in BAV patients with AS [164]. BAV patients undergoing ascending aortic resection received preoperative 4D flow MRI to regionally map 3D WSS and correlate these findings with histologic examination of surgically resected tissue samples. Paired aortic wall samples (i.e., regions of both elevated and normal WSS within the same patient) were collected and compared for medial elastin degeneration by histology. Regions of increased WSS showed greater medial elastin degradation compared to adjacent areas with normal WSS. Another study confirmed these results and showed that in the presence of aortic stenosis, the correlation between WSS and elastin fiber thickness was stronger than without AS [165]. These data suggest that regional valve-mediated hemodynamics could serve as potential prognostic biomarkers of aortic disease.

## Marfan Syndrome

Marfan syndrome is an inherited autosomal dominant connective tissue disease, mostly related to mutations in the fibrillin-1 (FBN1) gene. Many organ systems can be involved, but most life-threatening complications are related to the cardiovascular system and include aortic wall abnormalities leading to dissection and aortic rupture. Although the entire aorta may dilate in Marfan syndrome, the aortic root and the proximal descending aorta are prone for progressive dilation and dissection [166–168]. Few studies have investigated aortic WSS in MFS disease cohorts

[169–171]. Altered WSS was most pronounced in the proximal ascending aorta and the proximal descending aorta, which corresponds to locations where aortic dissection and rupture are most likely to occur. A recent longitudinal study in Marfan patient with baseline and mean follow-up 4D flow MRI (mean duration of $3.5 \pm 1.2$ years) confirmed these findings [169]. MFS patients had lower segmental WSS in the inner proximal DAo segment which correlated with increased localized aberrant vortex/helix flow patterns and an enlarged diameter. Aortic hemodynamics were stable over multi-year follow-up, but subtle localized flow changes in the descending aorta were already present at young age and tended to be more pronounced in the course of time. This is an important and intriguing finding, as the proximal descending aorta is a known initiation region for type B aortic dissections.

4D flow MRI was also used to calculate PWV as a measure for aortic stiffness in the aorta of BAV patients compared to controls and Marfan patients [172, 173]. Marfan patients had markedly higher aortic PWV and thus stiffer aortas compared to controls and BAV patients. The increased aortic stiffness may lead to further deterioration of aortic and LV function and may thus constitute important parameter for longitudinal monitoring of risk for progressive aortic dilation in these patients.

**Aortic Coarctation**

Aortic coarctation accounts for 6% of congenital cardiac malformations, is associated with hypertension and peripheral vascular disease, and often requires surgical repair [174]. This disease is characterized by a congenital narrowing of the aorta, usually at the level of the distal arch or proximal descending aorta. To provide insight into the degree of stenosis and impact on distal flow as a result of the coarctation, traditional assessment includes aorta diameter measurements and post-coarctation flow velocity assessment. Using 4D flow MRI to assess this cohort of patients has proven to provide useful characteristics about the impact of coarctation and coarctation repair on flow features throughout the aorta. Recent studies have shown that 4D flow MRI can measure and visualize alterations in 3D aortic hemodynamics in coarctation patients such as elevated helix and vortex flow throughout the entire aorta, including the region of repair [175–178]. Patients with aortic coarctation tend to have flow jet eccentricity following the coarctation resulting in jet impingement and elevated WSS along the descending aorta [179, 180].

**Aortic Atherosclerosis**

Stiffening of the aorta is frequently observed with increasing age and disease (e.g., hypertension, diabetes) due to an increase in the collagen-elastin ratio. Increased stiffness results in greater hemodynamic loading conditions on the aortic endothelium leading to the development of atherosclerosis [84, 181].

   The most commonly measured and best surrogate for arterial stiffness is pulse wave velocity (PWV) [85, 182, 183]. In 2 studies with 37 and 98 subjects, respectively, the reliability of 4D flow-based estimation of global aortic PWV was demonstrated in volunteers and patients with aortic atherosclerotic disease with a good observer dependence and excellent test-retest reliability [82, 184]. Both studies demonstrated significant correlations of aortic stiffness with age. In addition, in patients with atherosclerosis, the PWV was significantly increased compared with controls demonstrating the sensitivity of the technique to detect elevated aortic stiffness. In a recent study, 4D flow MRI-derived PWV parameters correlated significantly with echocardiographic stiffness parameters and intima-media thickness in the descending aorta of stroke patients [185]. Harloff et al. showed an increase in aortic PWV in older subjects that had more aortic plaque [186].

### Peripheral Arteries

Peripheral arterial occlusive disease (PAOD) is commonly explored with basic clinical tests such as the ankle-brachial-index, constant load treadmill test, and Doppler ultrasound due to its excellent temporal and spatial resolution. A number of studies have reported the use of 2D PC MRI for the quantitative assessment of PAOD severity [187–190]. Similar to Doppler ultrasound, the waveforms derived in locations superior or inferior to stenoses were being used to characterize the severity of PAOD [191, 192]. In a similar fashion, 4D flow MRI can be applied to the peripheral arteries, but only few studies have been reported to date. Application of this technique in the lower extremities has been limited to a single study which evaluated the iliac and proximal femoral at 3T [193]. Limitations of 4D flow in the extremities include the large anatomical coverage needed for vessel assessment, small vessel size (specially in distal vessels), and thus long scan times to achieve sufficient spatial resolution and SNR. Future research is warranted to extend previously published feasibility results to longitudinal and comparative studies investigating the potential impact of 4D flow MRI in PAOD.

## Future Directions and Conclusions

Recent developments related to highly accelerated 4D flow MRI have resulted in increased flexibility for the application of 4D flow MRI with reduced scan times and/or increased spatiotemporal resolutions. These developments have led to more widespread applications of 4D flow MRI, but further improvements in spatial resolution for the reliable quantification of vascular hemodynamics near the vessel wall or in small arteries affected are needed. 4D flow MRI acquisition at higher field strengths, e.g., 7T, and the associated increase in signal-to-noise ratio is promising in this regard. Studies have demonstrated that 7T 4D flow MRI allows for more detailed visualization of 3D velocity fields compared to 3T in the brain [125, 194]

and the aorta [195, 196]. However, 7T scanners are expensive and need tailor-made equipment and specialized operator expertise, which can hamper its clinical application. As an alternative, 4D flow image quality and velocity dynamic range can be improved by dual- or multi-VENC flow encoding. By combining a low-VENC acquisition with phase unwrapping guided by a simultaneous high-VENC acquisition, aliasing-free images can be acquired with high velocity-to-noise ratio [197]. By interleaving the high- and low-VENC acquisitions in combination with imaging acceleration techniques, dual-VENC 4D flow MRI has shown promise for detailed velocity measurements for neurovascular and aortic applications [198, 199]. Alternatively, additional velocity encoding steps further improved velocity-to-noise ratio, and velocity unwrapping can be added to standard acquisitions at the cost of extra scan time [27, 200, 201]. These methods showed improved aortic and neurovascular blood flow velocity visualization [202, 203].

PWV and WSS quantification are promising markers of vessel wall abnormalities but require laborious and time-consuming manual placement of analysis planes or segmentation of the 3D vessel lumen. To make 4D flow MRI data analysis more time-efficient, several groups have developed methods to automate these processing steps. For example, Bustamante et al. used advanced atlas-based methods for time-resolved aortic segmentation and plane placement [204]. The centerline of a 3D aortic segmentation can subsequently be used for automatic plane placement [151]. For 3D segmentation of the intracranial vasculature, highly automated algorithms were developed [205].

In conclusion, 4D flow MRI is a highly versatile technique which can be employed to derive important clinical parameters such as pulse wave velocity and wall shear stress in a large range of vessel wall diseases. Many studies have shown the additional value of 4D flow MRI in a clinical setting, but the methodology is still limitedly used for diagnosis or treatment planning in cardiovascular disease worldwide. Current and future efforts in the field are dedicated to the acceleration of the acquisition and the automated processing of the data, with the ultimate goal of developing 4D flow MRI in a widespread, easy-to-use clinical tool for vessel wall disease assessment.

# References

1. Carr HY, Purcell EM. Effects of diffusion on free precession in nuclear magnetic resonance experiments. Phys Rev. 1954;94:630–8.
2. Hahn EL. Detection of sea-water motion by nuclear precession. J Geophys Res. 1960;65:776–7.
3. Grant JP, Back C. NMR rheotomography: feasibility and clinical potential. Med Phys. 1982;9:188–93.
4. Moran PR. A flow velocity zeugmatographic interlace for NMR imaging in humans. Magn Reson Imaging. 1982;1:197–203.
5. Bryant DJ, Payne JA, Firmin DN, Longmore DB. Measurement of flow with NMR imaging using a gradient pulse and phase difference technique. J Comput Assist Tomogr. 1984;8:588–93.

6. van Dijk P. Direct cardiac NMR imaging of heart wall and blood flow velocity. J Comput Assist Tomogr. 1984;8:429–36.
7. Nayler GL, Firmin DN, Longmore DB. Blood flow imaging by cine magnetic resonance. J Comput Assist Tomogr. 1986;10:715–22.
8. Pelc NJ, Herfkens RJ, Shimakawa A, Enzmann DR. Phase contrast cine magnetic resonance imaging. Magn Reson Q. 1991;7:229–54.
9. Chai P, Mohiaddin R. How we perform cardiovascular magnetic resonance flow assessment using phase-contrast velocity mapping. J Cardiovasc Magn Reson. 2005;7:705–16.
10. Nayak KS, Nielsen J-F, Bernstein MA, Markl M, D Gatehouse P, M Botnar R, Saloner D, Lorenz C, Wen H, S Hu B, Epstein FH, N Oshinski J, Raman SV. Cardiovascular magnetic resonance phase contrast imaging. J Cardiovasc Magn Reson. 2015;17:71.
11. Markl M, Kilner PJ, Ebbers T. Comprehensive 4D velocity mapping of the heart and great vessels by cardiovascular magnetic resonance. J Cardiovasc Magn Reson. 2011;13:7.
12. Markl M, Frydrychowicz A, Kozerke S, Hope M, Wieben O. 4D flow MRI. J Magn Reson Imaging. 2012;36:1015–36.
13. Blanken CPS, Farag ES, Boekholdt SM, Leiner T, Kluin J, Nederveen AJ, van Ooij P, Planken RN. Advanced cardiac MRI techniques for evaluation of left-sided valvular heart disease. J Magn Reson Imaging. 2018;48:318–29.
14. O'Donnell M. NMR blood flow imaging using multiecho, phase contrast sequences. Med Phys. 1985;12:59–64.
15. Dumoulin CL, Souza SP, Walker MF, Wagle W. Three-dimensional phase contrast angiography. Magn Reson Med. 1989;9:139–49.
16. Mohiaddin RH, Yang GZ, Kilner PJ. Visualization of flow by vector analysis of multidirectional cine MR velocity mapping. J Comput Assist Tomogr. 1994;18:383–92.
17. Lenz GW, Haacke EM, White RD. Retrospective cardiac gating: a review of technical aspects and future directions. Magn Reson Imaging. 1989;7:445–55.
18. Markl M, Chan FP, Alley MT, Wedding KL, Draney MT, Elkins CJ, Parker DW, Wicker R, Taylor CA, Herfkens RJ, Pelc NJ. Time-resolved three-dimensional phase-contrast MRI. J Magn Reson Imaging. 2003;17:499–506.
19. Bogren HG, Klipstein RH, Firmin DN, Mohiaddin RH, Underwood SR, Rees RS, Longmore DB. Quantitation of antegrade and retrograde blood flow in the human aorta by magnetic resonance velocity mapping. Am Heart J. 1989;117:1214–22.
20. Caro CG, Dumoulin CL, Graham JM, Parker KH, Souza SP. Secondary flow in the human common carotid artery imaged by MR angiography. J Biomech Eng. 1992;114:147–9.
21. Marks MP, Pelc NJ, Ross MR, Enzmann DR. Determination of cerebral blood flow with a phase-contrast cine MR imaging technique: evaluation of normal subjects and patients with arteriovenous malformations. Radiology. 1992;182:467–76.
22. Wigstrom L, Sjoqvist L, Wranne B. Temporally resolved 3D phase-contrast imaging. Magn Reson Med. 1996;36:800–3.
23. Atkinson DJ, Edelman RR. Cineangiography of the heart in a single breath hold with a segmented turboFLASH sequence. Radiology. 1991;178:357–60.
24. Thomsen C, Cortsen M, Söndergaard L, Henriksen O, Ståhlberg F. A segmented K-space velocity mapping protocol for quantification of renal artery blood flow during breath-holding. J Magn Reson Imaging. 1995;5:393–401.
25. Pelc NJ, Bernstein MA, Shimakawa A, Glover GH. Encoding strategies for three-direction phase-contrast MR imaging of flow. J Magn Reson Imaging. 1991;1:405–13.
26. Bernstein MA, Shimakawa A, Pelc NJ. Minimizing TE in moment-nulled or flow-encoded two-and three-dimensional gradient-echo imaging. J Magn Reson Imaging. 1992;2:583–8.
27. Johnson KM, Markl M. Improved SNR in phase contrast velocimetry with five-point balanced flow encoding. Magn Reson Med. 2010;63:349–55.
28. Bock J, Kreher W, Hennig J, Markl M. Optimized pre-processing of time-resolved 2D and 3D phase contrast MRI data. Proc Int Soc Mag Reson Med. 2007;15:3138.
29. Firmin DN, Klipstein RH, Hounsfield GL, Paley MP, Longmore DB. Echo-planar high-resolution flow velocity mapping. Magn Reson Med. 1989;12:316–27.

30. Pruessmann KP, Weiger M, Scheidegger MB, Boesiger P. SENSE: sensitivity encoding for fast MRI. Magn Reson Med. 1999;42:952–62.
31. Thunberg P, Karlsson M, Wigstrom L. Accuracy and reproducibility in phase contrast imaging using SENSE. Magn Reson Med. 2003;50:1061–8.
32. Griswold MA, Jakob PM, Heidemann RM, Nittka M, Jellus V, Wang J, Kiefer B, Haase A. Generalized autocalibrating partially parallel acquisitions (GRAPPA). Magn Reson Med. 2002;47:1202–10.
33. Tsao J, Boesiger P, Pruessmann KP. k-t BLAST and k-t SENSE: dynamic MRI with high frame rate exploiting spatiotemporal correlations. Magn Reson Med. 2003;50:1031–42.
34. van Ooij P, Guedon A, Marquering HA, Schneiders JJ, Majoie CB, van Bavel E, Nederveen AJ. k-t BLAST and SENSE accelerated time-resolved three-dimensional phase contrast MRI in an intracranial aneurysm. MAGMA. 2013;26:261–70.
35. Schnell S, Markl M, Entezari P, Mahadewia RJ, Semaan E, Stankovic Z, Collins J, Carr J, Jung B. k-t GRAPPA accelerated four-dimensional flow MRI in the aorta: effect on scan time, image quality, and quantification of flow and wall shear stress. Magn Reson Med. 2014;72:522–33.
36. Pedersen H, Kozerke S, Ringgaard S, Nehrke K, Kim WY. k-t PCA: temporally constrained k-t BLAST reconstruction using principal component analysis. Magn Reson Med. 2009;62:706–16.
37. Giese D, Wong J, Greil GF, Buehrer M, Schaeffter T, Kozerke S. Towards highly accelerated Cartesian time-resolved 3D flow cardiovascular magnetic resonance in the clinical setting. J Cardiovasc Magn Reson. 2014;16:42.
38. Liu J, Koskas L, Faraji F, Kao E, Wang Y, Haraldsson H, Kefayati S, Zhu C, Ahn S, Laub G, Saloner D. Highly accelerated intracranial 4D flow MRI: evaluation of healthy volunteers and patients with intracranial aneurysms. MAGMA. 2018;31:295–307.
39. Lustig M, Donoho D, Pauly JM. Sparse MRI: the application of compressed sensing for rapid MR imaging. Magn Reson Med. 2007;58:1182–95.
40. Cheng JY, Hanneman K, Zhang T, Alley MT, Lai P, Tamir JI, Uecker M, Pauly JM, Lustig M, Vasanawala SS. Comprehensive motion-compensated highly accelerated 4D flow MRI with ferumoxytol enhancement for pediatric congenital heart disease. J Magn Reson Imaging. 2016;43:1355–68.
41. Bollache E, Barker AJ, Dolan RS, Carr JC, van Ooij P, Ahmadian R, Powell A, Collins JD, Geiger J, Markl M. k-t accelerated aortic 4D flow MRI in under two minutes: feasibility and impact of resolution, k-space sampling patterns, and respiratory navigator gating on hemodynamic measurements. Magn Reson Med. 2018;79:195–207.
42. Gu T, Korosec FR, Block WF, Fain SB, Turk Q, Lum D, Zhou Y, Grist TM, Haughton V, Mistretta CA. PC VIPR: a high-speed 3D phase-contrast method for flow quantification and high-resolution angiography. AJNR Am J Neuroradiol. 2005;26:743–9.
43. Glover GH, Pauly JM. Projection reconstruction techniques for reduction of motion effects in MRI. Magn Reson Med. 1992;28:275–89.
44. Ahn CB, Kim JH, Cho ZH. High-speed spiral-scan echo planar NMR imaging-I. IEEE Trans Med Imaging. 1986;5:2–7.
45. Dyvorne H, Knight-Greenfield A, Jajamovich G, Besa C, Cui Y, Stalder A, Markl M, Taouli B. Abdominal 4D flow MR imaging in a breath hold: combination of spiral sampling and dynamic compressed sensing for highly accelerated acquisition. Radiology. 2015;275:245–54.
46. Bastkowski R, Weiss K, Maintz D, Giese D. Self-gated golden-angle spiral 4D flow MRI. Magn Reson Med. 2018;80:904–13.
47. Petersson S, Sigfridsson A, Dyverfeldt P, Carlhäll CJ, Ebbers T. Retrospectively gated intracardiac 4D flow MRI using spiral trajectories. Magn Reson Med. 2016;75:196–206.
48. Haider CR, Hu HH, Campeau NG, Huston J, Riederer SJ. 3D high temporal and spatial resolution contrast-enhanced MR angiography of the whole brain. Magn Reson Med. 2008;60:749–60.
49. Liu J, Saloner D. Accelerated MRI with CIRcular Cartesian UnderSampling (CIRCUS): a variable density Cartesian sampling strategy for compressed sensing and parallel imaging. Quant Imaging Med Surg. 2014;4:57–67.

50. Cheng JY, Zhang T, Alley MT, Uecker M, Lustig M, Pauly JM, Vasanawala SS. Comprehensive multi-dimensional MRI for the simultaneous assessment of cardiopulmonary anatomy and physiology. Sci Rep. 2017;7:5330.

51. Runge VM, Clanton JA, Partain CL, James AE. Respiratory gating in magnetic resonance imaging at 0.5 Tesla. Radiology. 1984;151:521–3.

52. Wang Y, Rossman PJ, Grimm RC, Riederer SJ, Ehman RL. Navigator-echo-based real-time respiratory gating and triggering for reduction of respiration effects in three-dimensional coronary MR angiography. Radiology. 1996;198:55–60.

53. Bailes DR, Gilderdale DJ, Bydder GM, Collins AG, Firmin DN. Respiratory ordered phase encoding (ROPE): a method for reducing respiratory motion artefacts in MR imaging. J Comput Assist Tomogr. 1985;9:835–8.

54. Markl M, Harloff A, Bley TA, Zaitsev M, Jung B, Weigang E, Langer M, Hennig J, Frydrychowicz A. Time-resolved 3D MR velocity mapping at 3T: improved navigator-gated assessment of vascular anatomy and blood flow. J Magn Reson Imaging. 2007;25:824–31.

55. van Ooij P, Semaan E, Schnell S, Giri S, Stankovic Z, Carr J, Barker AJ, Markl M. Improved respiratory navigator gating for thoracic 4D flow MRI. Magn Reson Imaging. 2015;33:992–9.

56. Uribe S, Beerbaum P, Sorensen TS, Rasmusson A, Razavi R, Schaeffter T. Four-dimensional (4D) flow of the whole heart and great vessels using real-time respiratory self-gating. Magn Reson Med. 2009;62:984–92.

57. Kim WS, Mun CW, Kim DJ, Cho ZH. Extraction of cardiac and respiratory motion cycles by use of projection data and its applications to NMR imaging. Magn Reson Med. 1990;13:25–37.

58. Norris DG, Hutchison JMS. Concomitant magnetic field gradients and their effects on imaging at low magnetic field strengths. Magn Reson Imaging. 1990;8:33–7.

59. Jehenson P, Westphal M, Schuff N. Analytical method for the compensation of eddy-current effects induced by pulsed magnetic field gradients in NMR systems. J Magn Reson. 1990;90:264–78.

60. Bernstein MA, Zhou XJ, Polzin JA, King KF, Ganin A, Pelc NJ, Glover GH. Concomitant gradient terms in phase contrast MR: analysis and correction. Magn Reson Med. 1998;39:300–8.

61. Walker PG, Cranney GB, Scheidegger MB, Waseleski G, Pohost GM, Yoganathan AP. Semiautomated method for noise reduction and background phase error correction in MR phase velocity data. J Magn Reson Imaging. 1993;3:521–30.

62. Giese D, Haeberlin M, Barmet C, Pruessmann KP, Schaeffter T, Kozerke S. Analysis and correction of background velocity offsets in phase-contrast flow measurements using magnetic field monitoring. Magn Reson Med. 2012;67:1294–302.

63. Wigstrom L, Ebbers T, Fyrenius A, Karlsson M, Engvall J, Wranne B, Bolger AF. Particle trace visualization of intracardiac flow using time-resolved 3D phase contrast MRI. Magn Reson Med. 1999;41:793–9.

64. Mohiaddin RH, Yang GZ, Burger P, Firmin DN, Longmore DB. Automatic enhancement, animation, and segmentation of flow in peripheral arteries from MR phase-shift velocity mapping. J Comput Assist Tomogr. 1992;16:176–81.

65. Walker PG, Cranney GB, Grimes RY, Delatore J, Rectenwald J, Pohost GM, Yoganathan AP. Three-dimensional reconstruction of the flow in a human left heart by using magnetic resonance phase velocity encoding. Ann Biomed Eng. 1996;24:139–47.

66. Napel S, Lee DH, Frayne R, Rutt BK. Visualizing three-dimensional flow with simulated streamlines and three-dimensional phase-contrast MR imaging. J Magn Reson Imaging. 1992;2:143–53.

67. Buonocore MH. Visualizing blood flow patterns using streamlines, arrows, and particle paths. Magn Reson Med. 1998;40:210–26.

68. Hiratzka LF, Bakris GL, Beckman JA, Bersin RM, Carr VF, Casey DE Jr, Eagle KA, Hermann LK, Isselbacher EM, Kazerooni EA, Kouchoukos NT, Lytle BW, Milewicz DM, Reich DL, Sen S, Shinn JA, Svensson LG, Williams DM, American College of Cardiology Foundation/American Heart Association Task Force on Practice G, American Association for Thoracic S, American College of R, American Stroke A, Society of Cardiovascular A, Society for

Cardiovascular A, Interventions, Society of Interventional R, Society of Thoracic S, Society for Vascular M. 2010 ACCF/AHA/AATS/ACR/ASA/SCA/SCAI/SIR/STS/SVM guidelines for the diagnosis and management of patients with thoracic aortic disease. A report of the American College of Cardiology Foundation/American Heart Association Task Force on Practice Guidelines, A. J Am Coll Cardiol. 2010;55:e27–e129.

69. Elbaz MSM, Calkoen EE, Westenberg JJM, Lelieveldt BPF, Roest AAW, van der Geest RJ. Vortex flow during early and late left ventricular filling in normal subjects: quantitative characterization using retrospectively-gated 4D flow cardiovascular magnetic resonance and three-dimensional vortex core analysis. J Cardiovasc Magn Reson. 2014;16:78.

70. Hirtler D, Garcia J, Barker AJ, Geiger J. Assessment of intracardiac flow and vorticity in the right heart of patients after repair of tetralogy of Fallot by flow-sensitive 4D MRI. Eur Radiol. 2016;26:3598–607.

71. Lorenz R, Bock J, Barker AJ, von Knobelsdorff-Brenkenhoff F, Wallis W, Korvink JG, Bissell MM, Schulz-Menger J, Markl M. 4D flow magnetic resonance imaging in bicuspid aortic valve disease demonstrates altered distribution of aortic blood flow helicity. Magn Reson Med. 2014;71:1542–53.

72. von Knobelsdorff-Brenkenhoff F, Trauzeddel RF, Barker AJ, Gruettner H, Markl M, Schulz-Menger J. Blood flow characteristics in the ascending aorta after aortic valve replacement--a pilot study using 4D-flow MRI. Int J Cardiol. 2014;170:426–33.

73. Boussel L, Rayz V, Martin A, Acevedo-Bolton G, Lawton MT, Higashida R, Smith WS, Young WL, Saloner D. Phase-contrast magnetic resonance imaging measurements in intracranial aneurysms in vivo of flow patterns, velocity fields, and wall shear stress: comparison with computational fluid dynamics. Magn Reson Med. 2009;61:409–17.

74. Bieging ET, Frydrychowicz A, Wentland A, Landgraf BR, Johnson KM, Wieben O, Francois CJ. In vivo three-dimensional MR wall shear stress estimation in ascending aortic dilatation. J Magn Reson Imaging. 2011;33:589–97.

75. Ebbers T, Wigström L, Bolger AF, Engvall J, Karlsson M. Estimation of relative cardiovascular pressures using time-resolved three-dimensional phase contrast MRI. Magn Reson Med. 2001;45:872–9.

76. Bock J, Frydrychowicz A, Lorenz R, Hirtler D, Barker AJ, Johnson KM, Arnold R, Burkhardt H, Hennig J, Markl M. In vivo noninvasive 4D pressure difference mapping in the human aorta: phantom comparison and application in healthy volunteers and patients. Magn Reson Med. 2011;66:1079–88.

77. Barker AJ, van Ooij P, Bandi K, Garcia J, Albaghdadi M, McCarthy P, Bonow RO, Carr J, Collins J, Malaisrie SC, Markl M. Viscous energy loss in the presence of abnormal aortic flow. Magn Reson Med. 2014;72:620–8.

78. Elbaz MSM, van der Geest RJ, Calkoen EE, de Roos A, Lelieveldt BPF, Roest AAW, Westenberg JJM. Assessment of viscous energy loss and the association with three-dimensional vortex ring formation in left ventricular inflow: in vivo evaluation using four-dimensional flow MRI. Magn Reson Med. 2017;77:794–805.

79. Dyverfeldt P, Hope MD, Tseng EE, Saloner D. Magnetic resonance measurement of turbulent kinetic energy for the estimation of irreversible pressure loss in aortic stenosis. JACC Cardiovasc Imaging. 2013;6:64–71.

80. Zajac J, Eriksson J, Dyverfeldt P, Bolger AF, Ebbers T, Carlhäll C-J. Turbulent kinetic energy in normal and myopathic left ventricles. J Magn Reson Imaging. 2015;41:1021–9.

81. Westenberg JJM, de Roos A, Grotenhuis HB, Steendijk P, Hendriksen D, van den Boogaard PJ, van der Geest RJ, Bax JJ, Jukema JW, Reiber JHC. Improved aortic pulse wave velocity assessment from multislice two-directional in-plane velocity-encoded magnetic resonance imaging. J Magn Reson Imaging. 2010;32:1086–94.

82. Markl M, Wallis W, Brendecke S, Simon J, Frydrychowicz A, Harloff A. Estimation of global aortic pulse wave velocity by flow-sensitive 4D MRI. Magn Reson Med. 2010;63:1575–82.

83. Geddes LA, Voelz MH, Babbs CF, Bourland JD, Tacker WA. Pulse transit time as an indicator of arterial blood pressure. Psychophysiology. 1981;18:71–4.

84. Blacher J, Safar ME. Large-artery stiffness, hypertension and cardiovascular risk in older patients. Nat Clin Pract Cardiovasc Med. 2005;2:450–5.

85. Wentland AL, Grist TM, Wieben O. Review of MRI-based measurements of pulse wave velocity: a biomarker of arterial stiffness. Cardiovasc Diagn Ther. 2014;4:193–206.

86. Vlachopoulos C, Aznaouridis K, Stefanadis C. Prediction of cardiovascular events and all-cause mortality with arterial stiffness: a systematic review and meta-analysis. J Am Coll Cardiol. 2010;55:1318–27.

87. Ait-Oufella H, Collin C, Bozec E, Laloux B, Ong K-T, Dufouil C, Boutouyrie P, Laurent S. Long-term reduction in aortic stiffness: a 5.3-year follow-up in routine clinical practice. J Hypertens. 2010;28:2336–41.

88. Saito T, Saito T, Sugiyama S, Asai K, Yasutake M, Mizuno K. Effects of long-term treatment for obstructive sleep apnea on pulse wave velocity. Hypertens Res. 2010;33:844–9.

89. Reference Values for Arterial Stiffness' Collaboration. Determinants of pulse wave velocity in healthy people and in the presence of cardiovascular risk factors: 'establishing normal and reference values.'. Eur Heart J. 2010;31:2338–50.

90. Mohiaddin RH, Firmin DN, Longmore DB. Age-related changes of human aortic flow wave velocity measured noninvasively by magnetic resonance imaging. J Appl Physiol. 1993;74:492–7.

91. Ibrahim E-SH, Johnson KR, Miller AB, Shaffer JM, White RD. Measuring aortic pulse wave velocity using high-field cardiovascular magnetic resonance: comparison of techniques. J Cardiovasc Magn Reson. 2010;12:26.

92. Hardy CJ, Bolster BD, McVeigh ER, Adams WJ, Zerhouni EA. A one-dimensional velocity technique for NMR measurement of aortic distensibility. Magn Reson Med. 1994;31:513–20.

93. Mohiaddin RH, Longmore DB. MRI studies of atherosclerotic vascular disease: structural evaluation and physiological measurements. Br Med Bull. 1989;45:968–90.

94. Yu H-Y, Peng H-H, Wang J-L, Wen C-Y, Tseng W-YI. Quantification of the pulse wave velocity of the descending aorta using axial velocity profiles from phase-contrast magnetic resonance imaging. Magn Reson Med. 2006;56:876–83.

95. Fielden SW, Fornwalt BK, Jerosch-Herold M, Eisner RL, Stillman AE, Oshinski JN. A new method for the determination of aortic pulse wave velocity using cross-correlation on 2D PCMR velocity data. J Magn Reson Imaging. 2008;27:1382–7.

96. Dyverfeldt P, Ebbers T, Länne T. Pulse wave velocity with 4D flow MRI: systematic differences and age-related regional vascular stiffness. Magn Reson Imaging. 2014;32:1266–71.

97. Malek AM, Jackman R, Rosenberg RD, Izumo S. Endothelial expression of thrombomodulin is reversibly regulated by fluid shear stress. Circ Res. 1994;74:852–60.

98. Lehoux S, Tedgui A. Cellular mechanics and gene expression in blood vessels. J Biomech. 2003;36:631–43.

99. Cheng C, Tempel D, van Haperen R, van der Baan A, Grosveld F, Daemen MJAP, Krams R, de Crom R. Atherosclerotic lesion size and vulnerability are determined by patterns of fluid shear stress. Circulation. 2006;113:2744–53.

100. Bissell MM, Hess AT, Biasiolli L, Glaze SJ, Loudon M, Pitcher A, Davis A, Prendergast B, Markl M, Barker AJ, Neubauer S, Myerson SG. Aortic dilation in bicuspid aortic valve disease: flow pattern is a major contributor and differs with valve fusion type. Circ Cardiovasc Imaging. 2013;6:499–507.

101. Mahadevia R, Barker AJ, Schnell S, Entezari P, Kansal P, Fedak PW, Malaisrie SC, McCarthy P, Collins J, Carr J, Markl M. Bicuspid aortic cusp fusion morphology alters aortic three-dimensional outflow patterns, wall shear stress, and expression of aortopathy. Circulation. 2014;129:673–82.

102. Malek AM, Alper SL, Izumo S. Hemodynamic shear stress and its role in atherosclerosis. JAMA. 1999;282:2035–42.

103. Dolan JM, Kolega J, Meng H. High wall shear stress and spatial gradients in vascular pathology: a review. Ann Biomed Eng. 2013;41:1411–27.

104. Boussel L, Rayz V, McCulloch C, Martin A, Acevedo-Bolton G, Lawton M, Higashida R, Smith WS, Young WL, Saloner D. Aneurysm growth occurs at region of low wall shear

stress: patient-specific correlation of hemodynamics and growth in a longitudinal study. Stroke. 2008;39:2997–3002.

105. Stalder A, Russe M, Frydrychowicz A, Bock J, Hennig J, Markl M. Quantitative 2D and 3D phase contrast MRI: optimized analysis of blood flow and vessel wall parameters. Magn Reson Med. 2008;60:1218–31.

106. Ku DN, Giddens DP, Zarins CK, Glagov S. Pulsatile flow and atherosclerosis in the human carotid bifurcation. Positive correlation between plaque location and low oscillating shear stress. Arteriosclerosis. 1985;5:293–302.

107. Van Ooij P, Potters WV, Guédon A, Schneiders JJ, Marquering HA, Majoie CB, Vanbavel E, Nederveen AJ. Wall shear stress estimated with phase contrast MRI in an in vitro and in vivo intracranial aneurysm. J Magn Reson Imaging. 2013;38:876–84.

108. Chang W, Loecher MW, Wu Y, Niemann DB, Ciske B, Aagaard-Kienitz B, Kecskemeti S, Johnson KM, Wieben O, Mistretta C, Turski P. Hemodynamic changes in patients with arteriovenous malformations assessed using high-resolution 3D radial phase-contrast MR angiography. AJNR Am J Neuroradiol. 2012;33:1565–72.

109. Potters WV, van Ooij P, Marquering HA, VanBavel E, Nederveen AJ. Volumetric arterial wall shear stress calculation based on cine phase contrast MRI. J Magn Reson Imaging. 2015;41:505–16.

110. Ziegler M, Lantz J, Ebbers T, Dyverfeldt P. Assessment of turbulent flow effects on the vessel wall using four-dimensional flow MRI. Magn Reson Med. 2017;77:2310–9.

111. van Ooij P, Garcia J, Potters WV, Malaisrie SC, Collins JD, Carr JC, Markl M, Barker AJ. Age-related changes in aortic 3D blood flow velocities and wall shear stress: implications for the identification of altered hemodynamics in patients with aortic valve disease. J Magn Reson Imaging. 2016;43:1239–49.

112. van Ooij P, Potters WV, Collins J, Carr M, Carr J, Malaisrie SC, Fedak PWM, McCarthy PM, Markl M, Barker AJ. Characterization of abnormal wall shear stress using 4D flow MRI in human bicuspid aortopathy. Ann Biomed Eng. 2015;43:1385–97.

113. Markl M, Wallis W, Harloff A. Reproducibility of flow and wall shear stress analysis using flow-sensitive four-dimensional MRI. J Magn Reson Imaging. 2011;33:988–94.

114. van Ooij P, Powell AL, Potters WV, Carr JC, Markl M, Barker AAJ. Reproducibility and interobserver variability of systolic blood flow velocity and 3D wall shear stress derived from 4D flow MRI in the healthy aorta. J Magn Reson Imaging. 2016;43:236–48.

115. Schubert T, Bieri O, Pansini M, Stippich C, Santini F. Peak velocity measurements in tortuous arteries with phase contrast magnetic resonance imaging: the effect of multidirectional velocity encoding. Investig Radiol. 2014;49:189–94.

116. Wetzel S, Meckel S, Frydrychowicz A, Bonati L, Radue EW, Scheffler K, Hennig J, Markl M. In vivo assessment and visualization of intracranial arterial hemodynamics with flow-sensitized 4D MR imaging at 3T. AJNR Am J Neuroradiol. 2007;28:433–8.

117. Václavů L, Baldew ZAV, Gevers S, Mutsaerts HJMM, Fijnvandraat K, Cnossen MH, Majoie CB, Wood JC, VanBavel E, Biemond BJ, van Ooij P, Nederveen AJ. Intracranial 4D flow magnetic resonance imaging reveals altered haemodynamics in sickle cell disease. Br J Haematol. 2018;180:432–42.

118. Isoda H, Ohkura Y, Kosugi T, Hirano M, Alley MT, Bammer R, Pelc NJ, Namba H, Sakahara H. Comparison of hemodynamics of intracranial aneurysms between MR fluid dynamics using 3D cine phase-contrast MRI and MR-based computational fluid dynamics. Neuroradiology. 2010;52:913–20.

119. Hope TA, Hope MD, Purcell DD, von Morze C, Vigneron DB, Alley MT, Dillon WP. Evaluation of intracranial stenoses and aneurysms with accelerated 4D flow. Magn Reson Imaging. 2010;28:41–6.

120. Chang W, Landgraf B, Johnson KM, Kecskemeti S, Wu Y, Velikina J, Rowley H, Wieben O, Mistretta C, Turski P. Velocity measurements in the middle cerebral arteries of healthy volunteers using 3D radial phase-contrast HYPRFlow: comparison with transcranial doppler sonography and 2D phase-contrast MR imaging. AJNR Am J Neuroradiol. 2011;32:54–9.

121. van Ooij P, Schneiders JJ, Marquering HA, Majoie CB, van Bavel E, Nederveen AJ. 3D cine phase-contrast MRI at 3T in intracranial aneurysms compared with patient-specific computational fluid dynamics. AJNR Am J Neuroradiol. 2013;34:1785–91.

122. Chang W, Wu Y, Johnson K, Loecher M, Wieben O, Edjlali M, Oppenheim C, Roca P, Hald J, Aagaard-Kienitz B, Niemann D, Mistretta C, Turski P. Fast contrast-enhanced 4D MRA and 4D flow MRI using constrained reconstruction (HYPRFlow): potential applications for brain arteriovenous malformations. AJNR Am J Neuroradiol. 2015;36:1049–55.

123. Ansari SA, Schnell S, Carroll T, Vakil P, Hurley MC, Wu C, Carr J, Bendok BR, Batjer H, Markl M. Intracranial 4D flow MRI: toward individualized assessment of arteriovenous malformation hemodynamics and treatment-induced changes. AJNR Am J Neuroradiol. 2013;34:1922–8.

124. Wu C, Ansari SA, Honarmand AR, Vakil P, Hurley MC, Bendok BR, Carr J, Carroll TJ, Markl M. Evaluation of 4D vascular flow and tissue perfusion in cerebral arteriovenous malformations: influence of Spetzler-Martin grade, clinical presentation, and AVM risk factors. AJNR Am J Neuroradiol. 2015;36:1142–9.

125. van Ooij P, Zwanenburg JJM, Visser F, Majoie CB, VanBavel E, Hendrikse J, Nederveen AJ. Quantification and visualization of flow in the circle of Willis: time-resolved three-dimensional phase contrast MRI at 7 T compared with 3 T. Magn Reson Med. 2013;69:868–76.

126. Cebral JR, Castro MA, Burgess JE, Pergolizzi RS, Sheridan MJ, Putman CM. Characterization of cerebral aneurysms for assessing risk of rupture by using patient-specific computational hemodynamics models. AJNR Am J Neuroradiol. 2005;26:2550–9.

127. Hassan T, Ezura M, Timofeev EV, Tominaga T, Saito T, Takahashi A, Takayama K, Yoshimoto T. Computational simulation of therapeutic parent artery occlusion to treat giant vertebro-basilar aneurysm. AJNR Am J Neuroradiol. 2004;25:63–8.

128. Jou LD, Quick CM, Young WL, Lawton MT, Higashida R, Martin A, Saloner D. Computational approach to quantifying hemodynamic forces in giant cerebral aneurysms. AJNR Am J Neuroradiol. 2003;24:1804–10.

129. Steinman DA, Milner JS, Norley CJ, Lownie SP, Holdsworth DW. Image-based computational simulation of flow dynamics in a giant intracranial aneurysm. AJNR Am J Neuroradiol. 2003;24:559–66.

130. Tateshima S, Murayama Y, Villablanca JP, Morino T, Nomura K, Tanishita K, Viñuela F. In vitro measurement of fluid-induced wall shear stress in unruptured cerebral aneurysms harboring blebs. Stroke. 2003;34:187–92.

131. Castro MA, Putman CM, Cebral JR. Computational fluid dynamics modeling of intracranial aneurysms: effects of parent artery segmentation on intra-aneurysmal hemodynamics. AJNR Am J Neuroradiol. 2006;27:1703–9.

132. Isoda H, Ohkura Y, Kosugi T, Hirano M, Takeda H, Hiramatsu H, Yamashita S, Takehara Y, Alley M, Bammer R, Pelc N, Namba H, Sakahara H. In vivo hemodynamic analysis of intracranial aneurysms obtained by magnetic resonance fluid dynamics (MRFD) based on time-resolved three-dimensional phase-contrast MRI. Neuroradiology. 2010;52:921–8.

133. Rayz VL, Boussel L, Ge L, Leach JR, Martin AJ, Lawton MT, McCulloch C, Saloner D. Flow residence time and regions of intraluminal thrombus deposition in intracranial aneurysms. Ann Biomed Eng. 2010;38:3058–69.

134. Meckel S, Stalder AF, Santini F, Radü E-W, Rüfenacht DA, Markl M, Wetzel SG. In vivo visualization and analysis of 3-D hemodynamics in cerebral aneurysms with flow-sensitized 4-D MR imaging at 3 T. Neuroradiology. 2008;50:473–84.

135. Kecskemeti S, Johnson K, Wu Y, Mistretta C, Turski P, Wieben O. High resolution three-dimensional cine phase contrast MRI of small intracranial aneurysms using a stack of stars k-space trajectory. J Magn Reson Imaging. 2011; https://doi.org/10.1002/jmri.23501.

136. Schnell S, Ansari SA, Vakil P, Wasielewski M, Carr ML, Hurley MC, Bendok BR, Batjer H, Carroll TJ, Carr J, Markl M. Three-dimensional hemodynamics in intracranial aneurysms: influence of size and morphology. J Magn Reson Imaging. 2014;39:120–31.

137. Blankena R, Kleinloog R, Verweij BH, Van Ooij P, Ten Haken B, Luijten PR, Rinkel GJE, Zwanenburg JJM. Thinner regions of intracranial aneurysm wall correlate with regions of higher wall shear stress: a 7T MRI study. Am J Neuroradiol. 2016;37:1310–7.

138. Lee SW, Antiga L, Spence JD, Steinman DA. Geometry of the carotid bifurcation predicts its exposure to disturbed flow. Stroke. 2008;39:2341–7.

139. Markl M, Wegent F, Zech T, Bauer S, Strecker C, Schumacher M, Weiller C, Hennig J, Harloff A. In vivo wall shear stress distribution in the carotid artery: effect of bifurcation geometry, internal carotid artery stenosis, and recanalization therapy. Circ Cardiovasc Imaging. 2010;3:647–55.

140. Cibis M, Potters WV, Gijsen FJ, Marquering H, vanBavel E, van der Steen AF, Nederveen AJ, Wentzel JJ. Wall shear stress calculations based on 3D cine phase contrast MRI and computational fluid dynamics: a comparison study in healthy carotid arteries. NMR Biomed. 2014;27:826–34.

141. Cibis M, Potters WV, Selwaness M, Gijsen FJ, Franco OH, Arias Lorza AM, de Bruijne M, Hofman A, van der Lugt A, Nederveen AJ, Wentzel JJ. Relation between wall shear stress and carotid artery wall thickening MRI versus CFD. J Biomech. 2016;49:735–41.

142. van Ooij P, Cibis M, Rowland EM, Vernooij MW, van der Lugt A, Weinberg PD, Wentzel JJ, Nederveen AJ. Spatial correlations between MRI-derived wall shear stress and vessel wall thickness in the carotid bifurcation. Eur Radiol Exp. 2018;2:27.

143. Stokholm R, Oyre S, Ringgaard S, Flaagoy H, Paaske WP, Pedersen EM. Determination of wall shear rate in the human carotid artery by magnetic resonance techniques. Eur J Vasc Endovasc Surg. 2000;20:427–33.

144. Gelfand BD, Epstein FH, Blackman BR. Spatial and spectral heterogeneity of time-varying shear stress profiles in the carotid bifurcation by phase-contrast MRI. J Magn Reson Imaging. 2006;24:1386–92.

145. Harloff A, Berg S, Barker AJ, Schöllhorn J, Schumacher M, Weiller C, Markl M. Wall shear stress distribution at the carotid bifurcation: influence of eversion carotid endarterectomy. Eur Radiol. 2013;23:3361–9.

146. Harloff A, Albrecht F, Spreer J, Stalder A, Bock J, Frydrychowicz A, Schöllhorn J, Hetzel A, Schumacher M, Hennig J, Markl M. 3D blood flow characteristics in the carotid artery bifurcation assessed by flow-sensitive 4D MRI at 3T. Magn Reson Med. 2009;61:65–74.

147. Kroner ES, Lamb HJ, Siebelink HM, Cannegieter SC, van den Boogaard PJ, van der Wall EE, de Roos A, Westenberg JJ. Pulse wave velocity and flow in the carotid artery versus the aortic arch: effects of aging. J Magn Reson Imaging. 2014;40:287–93.

148. Peper ES, Strijkers GJ, Gazzola K, Potters WV, Motaal AG, Luirink IK, Hutten BA, Wiegman A, van Ooij P, van den Born B-JH, Nederveen AJ, Coolen BF. Regional assessment of carotid artery pulse wave velocity using compressed sensing accelerated high temporal resolution 2D CINE phase contrast cardiovascular magnetic resonance. J Cardiovasc Magn Reson. 2018;20:86.

149. Sigovan M, Hope MD, Dyverfeldt P, Saloner D. Comparison of four-dimensional flow parameters for quantification of flow eccentricity in the ascending aorta. J Magn Reson Imaging. 2011;34:1226–30.

150. Burris NS, Sigovan M, Knauer HA, Tseng EE, Saloner D, Hope MD. Systolic flow displacement correlates with future ascending aortic growth in patients with bicuspid aortic valves undergoing magnetic resonance surveillance. Investig Radiol. 2014;49:635–9.

151. Garcia J, Barker AJ, Murphy I, Jarvis K, Schnell S, Collins JD, Carr JC, Malaisrie SC, Markl M. Four-dimensional flow magnetic resonance imaging-based characterization of aortic morphometry and haemodynamics: impact of age, aortic diameter, and valve morphology. Eur Hear J Cardiovasc Imaging. 2015. jev228

152. Hope MD, Sigovan M, Wrenn SJ, Saloner D, Dyverfeldt P. MRI hemodynamic markers of progressive bicuspid aortic valve-related aortic disease. J Magn Reson Imaging. 2014;40:140–5.

153. Raghav V, Barker AJ, Mangiameli D, Mirabella L, Markl M, Yoganathan AP. Valve mediated hemodynamics and their association with distal ascending aortic diameter in bicuspid aortic valve subjects. J Magn Reson Imaging. 2018;47:246–54.

154. Kauhanen SP, Hedman M, Kariniemi E, Jaakkola P, Vanninen R, Saari P, Liimatainen T. Aortic dilatation associates with flow displacement and increased circumferential wall shear stress in patients without aortic stenosis: a prospective clinical study. J Magn Reson Imaging. 2019; https://doi.org/10.1002/jmri.26655.

155. Rodríguez-Palomares JF, Dux-Santoy L, Guala A, Kale R, Maldonado G, Teixidó-Turà G, Galian L, Huguet M, Valente F, Gutiérrez L, González-Alujas T, Johnson KM, Wieben O, García-Dorado D, Evangelista A. Aortic flow patterns and wall shear stress maps by 4D-flow cardiovascular magnetic resonance in the assessment of aortic dilatation in bicuspid aortic valve disease. J Cardiovasc Magn Reson. 2018;20:28.

156. Burk J, Blanke P, Stankovic Z, Barker A, Russe M, Geiger J, Frydrychowicz A, Langer M, Markl M. Evaluation of 3D blood flow patterns and wall shear stress in the normal and dilated thoracic aorta using flow-sensitive 4D CMR. J Cardiovasc Magn Reson. 2012;14:84.

157. Harloff A, Nussbaumer A, Bauer S, Stalder AF, Frydrychowicz A, Weiller C, Hennig J, Markl M. In vivo assessment of wall shear stress in the atherosclerotic aorta using flow-sensitive 4D MRI. Magn Reson Med. 2010;63:1529–36.

158. Hope MD, Hope TA, Crook SE, Ordovas KG, Urbania TH, Alley MT, Higgins CB. 4D flow CMR in assessment of valve-related ascending aortic disease. JACC Cardiovasc Imaging. 2011;4:781–7.

159. Barker AJ, Markl M, Burk J, Lorenz R, Bock J, Bauer S, Schulz-Menger J, von Knobelsdorff-Brenkenhoff F. Bicuspid aortic valve is associated with altered wall shear stress in the ascending aorta. Circ Cardiovasc Imaging. 2012;5:457–66.

160. Meierhofer C, Schneider EP, Lyko C, Hutter A, Martinoff S, Markl M, Hager A, Hess J, Stern H, Fratz S. Wall shear stress and flow patterns in the ascending aorta in patients with bicuspid aortic valves differ significantly from tricuspid aortic valves: a prospective study. Eur Heart J Cardiovasc Imaging. 2012;14:797–804.

161. Shan Y, Li J, Wang Y, Wu B, Barker AJ, Markl M, Wang C, Wang X, Shu X. Aortic shear stress in patients with bicuspid aortic valve with stenosis and insufficiency. J Thorac Cardiovasc Surg. 2017;153:1263–1272.e1.

162. van Ooij P, Markl M, Collins JD, Carr JC, Rigsby C, Bonow RO, Chris Malaisrie S, McCarthy PM, Fedak PWM, Barker AJ. Aortic valve stenosis alters expression of regional aortic wall shear stress: new insights from a 4-dimensional flow magnetic resonance imaging study of 571 subjects. J Am Heart Assoc. 2017;6:1–14.

163. van Ooij P, Markl M, Collins JD, Carr JC, Malaisrie SC, McCarthy PM, Nederveen AJ, Fedak PWM, Barker AJ. Mapping of abnormal aortic hemodynamics in 515 patients with aortopathy. Proc Int Soc Mag Reson. 2017;25:0754.

164. Guzzardi DG, Barker AJ, van Ooij P, Malaisrie SC, Puthumana JJ, Belke DD, Mewhort HEM, Svystonyuk DA, Kang S, Verma S, Collins J, Carr J, Bonow RO, Markl M, Thomas JD, Mccarthy PM, Fedak PWM. Valve-related hemodynamics mediate human bicuspid aortopathy: insights from wall shear stress mapping. J Am Coll Cardiol. 2015;66:892–900.

165. Bollache E, Guzzardi DG, Sattari S, Olsen KE, Di Martino ES, Malaisrie SC, van Ooij P, Collins J, Carr J, McCarthy PM, Markl M, Barker AJ, Fedak PWM. Aortic valve-mediated wall shear stress is heterogeneous and predicts regional aortic elastic fiber thinning in bicuspid aortic valve-associated aortopathy. J Thorac Cardiovasc Surg. 2018;156:2112–2120.e2.

166. Alpendurada F, Mohiaddin R. 1039 prevalence of cardiovascular manifestations in patients with Marfan syndrome: a cardiovascular magnetic resonance study. J Cardiovasc Magn Reson. 2008;10:A164.

167. Engelfriet PM, Boersma E, Tijssen JGP, Bouma BJ, Mulder BJM. Beyond the root: dilatation of the distal aorta in Marfan's syndrome. Heart. 2006;92:1238–43.

168. Mariucci EM, Lovato L, Rosati M, Palena LM, Bonvicini M, Fattori R. Dilation of peripheral vessels in Marfan syndrome: importance of thoracoabdominal MR angiography. Int J Cardiol. 2013;167:2928–31.

169. Geiger J, Hirtler D, Gottfried K, Rahman O, Bollache E, Barker AJ, Markl M, Stiller B. Longitudinal evaluation of aortic hemodynamics in Marfan syndrome: new insights from a 4D flow cardiovascular magnetic resonance multi-year follow-up study. J Cardiovasc Magn Reson. 2017;19:33.

170. van der Palen RLF, Barker AJ, Bollache E, Garcia J, Rose MJ, van Ooij P, Young LT, Roest AAW, Markl M, Robinson JD, Rigsby CK. Altered aortic 3D hemodynamics and geometry in pediatric Marfan syndrome patients. J Cardiovasc Magn Reson. 2017;19:30.

171. Wang H-H, Chiu H-H, Tseng W-YI, Peng H-H. Does altered aortic flow in marfan syndrome relate to aortic root dilatation? J Magn Reson Imaging. 2016;44:500–8.

172. Kröner ESJ, Scholte AJHA, de Koning PJH, van den Boogaard PJ, Kroft LJM, van der Geest RJ, Hilhorst-Hofstee Y, Lamb HJ, Siebelink H-MJ, Mulder BJM, Groenink M, Radonic T, van der Wall EE, de Roos A, Reiber JHC, Westenberg JJM. MRI-assessed regional pulse wave velocity for predicting absence of regional aorta luminal growth in marfan syndrome. Int J Cardiol. 2013;167:2977–82.

173. Guala A, Rodriguez-Palomares J, Dux-Santoy L, Teixido-Tura G, Maldonado G, Galian L, Huguet M, Valente F, Gutiérrez L, González-Alujas T, Johnson KM, Wieben O, Sao Avilés A, Garcia-Dorado D, Evangelista A. Influence of aortic dilation on the regional aortic stiffness of bicuspid aortic valve assessed by 4-dimensional flow cardiac magnetic resonance: comparison with Marfan syndrome and degenerative aortic aneurysm. JACC Cardiovasc Imaging. 2018; https://doi.org/10.1016/j.jcmg.2018.03.017.

174. Abbruzzese PA, Aidala E. Aortic coarctation: an overview. J Cardiovasc Med (Hagerstown). 2007;8:123–8.

175. Hope MD, Meadows AK, Hope TA, Ordovas KG, Saloner D, Reddy GP, Alley MT, Higgins CB. Clinical evaluation of aortic coarctation with 4D flow MR imaging. J Magn Reson Imaging. 2010;31:711–8.

176. Frydrychowicz A, Markl M, Hirtler D, Harloff A, Schlensak C, Geiger J, Stiller B, Arnold R. Aortic hemodynamics in patients with and without repair of aortic coarctation: in vivo analysis by 4D flow-sensitive magnetic resonance imaging. Investig Radiol. 2011;46:317–25.

177. Riesenkampff E, Fernandes JF, Meier S, Goubergrits L, Kropf S, Schubert S, Berger F, Henneumuth A, Kuehne T. Pressure fields by flow-sensitive, 4D, velocity-encoded CMR in patients with aortic coarctation. JACC Cardiovasc Imaging. 2014;7:920–6.

178. Vasanawala SS, Hanneman K, Alley MT, Hsiao A. Congenital heart disease assessment with 4D flow MRI. J Magn Reson Imaging. 2015;42:870–86.

179. Allen BD, Barker AJ, Carr JC, Silverberg RA, Markl M. Time-resolved three-dimensional phase contrast MRI evaluation of bicuspid aortic valve and coarctation of the aorta. Eur Heart J Cardiovasc Imaging. 2013;14:399.

180. Farag ES, van Ooij P, Boekholdt SM, Planken RN, Dukker KC, Bouma BJ, Groenink M, Koolbergen DR, Sojak V, Nederveen AJ, Hazekamp MG, de Mol BA, Kluin J. Abnormal blood flow and wall shear stress are present in corrected aortic coarctation despite successful surgical repair. J Cardiovasc Surg. 2019;60:152–4.

181. Janić M, Lunder M, Sabovič M. Arterial stiffness and cardiovascular therapy. Biomed Res Int. 2014;2014:621437.

182. Tomiyama H, Yamashina A. Non-invasive vascular function tests: their pathophysiological background and clinical application. Circ J. 2010;74:24–33.

183. Sethi S, Rivera O, Oliveros R, Chilton R. Aortic stiffness: pathophysiology, clinical implications, and approach to treatment. Integr Blood Press Control. 2014;7:29–34.

184. Markl M, Wallis W, Strecker C, Gladstone BP, Vach W, Harloff A. Analysis of pulse wave velocity in the thoracic aorta by flow-sensitive four-dimensional MRI: reproducibility and correlation with characteristics in patients with aortic atherosclerosis. J Magn Reson Imaging. 2012;35:1162–8.

185. Wehrum T, Günther F, Kams M, Wendel S, Strecker C, Mirzaee H, Harloff A. Quantification of aortic stiffness in stroke patients using 4D flow MRI in comparison with transesophageal echocardiography. Int J Cardiovasc Imaging. 2018;34:1629–36.

186. Harloff A, Mirzaee H, Lodemann T, Hagenlocher P, Wehrum T, Stuplich J, Hennemuth A, Hennig J, Grundmann S, Vach W. Determination of aortic stiffness using 4D flow cardiovascular magnetic resonance - a population-based study. J Cardiovasc Magn Reson. 2018;20:43.

187. Goyen M, Heuser LJ. Improved peripheral MRA using multi-velocity-encoding phase contrast-enhanced MRA techniques. Acta Radiol. 2000;41:139–41.

188. Steffens JC, Link J, Müller-Hülsbeck S, Freund M, Brinkmann G, Heller M. Cardiac-gated two-dimensional phase-contrast MR angiography of lower extremity occlusive disease. AJR Am J Roentgenol. 1997;169:749–54.

189. Swan JS, Grist TM, Weber DM, Sproat IA, Wojtowycz MM. MR angiography of the pelvis with variable velocity encoding and a phased-array coil. Radiology. 1994;190:363–9.

190. Yucel EK, Dumoulin CL, Waltman AC. MR angiography of lower-extremity arterial disease: preliminary experience. J Magn Reson Imaging. 1992;2:303–9.

191. Krug B, Kugel H, Friedmann G, Bunke J, van Dijk P, Schmidt R, Hirche HJ. MR imaging of poststenotic flow phenomena: experimental studies. J Magn Reson Imaging. 1991;1:585–91.

192. Krug B, Kugel H, Harnischmacher U, Heindel W, Schmidt R, Krings F. MR pulsatility measurements in peripheral arteries: preliminary results. Magn Reson Med. 1995;34:698–705.

193. Frydrychowicz A, Winterer JT, Zaitsev M, Jung B, Hennig J, Langer M, Markl M. Visualization of iliac and proximal femoral artery hemodynamics using time-resolved 3D phase contrast MRI at 3T. J Magn Reson Imaging. 2007;25:1085–92.

194. Kang C-K, Park C-A, Lee DS, Lee Y-B, Park C-W, Kim Y-B, Cho Z-H. Velocity measurement of microvessels using phase-contrast magnetic resonance angiography at 7 Tesla MRI. Magn Reson Med. 2016;75:1640–6.

195. Hess AT, Bissell MM, Ntusi NAB, Lewis AJM, Tunnicliffe EM, Greiser A, Stalder AF, Francis JM, Myerson SG, Neubauer S, Robson MD. Aortic 4D flow: quantification of signal-to-noise ratio as a function of field strength and contrast enhancement for 1.5T, 3T, and 7T. Magn Reson Med. 2014. n/a-n/a.

196. Schmitter S, Schnell S, Uğurbil K, Markl M, Van de Moortele P-F. Towards high-resolution 4D flow MRI in the human aorta using kt-GRAPPA and B1+ shimming at 7T. J Magn Reson Imaging. 2016;44:486–99.

197. Nett EJ, Johnson KM, Frydrychowicz A, Del Rio AM, Schrauben E, Francois CJ, Wieben O. Four-dimensional phase contrast MRI with accelerated dual velocity encoding. J Magn Reson Imaging. 2012; https://doi.org/10.1002/jmri.23588.

198. Schnell S, Ansari SA, Wu C, Garcia J, Murphy IG, Rahman OA, Rahsepar AA, Aristova M, Collins JD, Carr JC, Markl M. Accelerated dual-venc 4D flow MRI for neurovascular applications. J Magn Reson Imaging. 2017;46:102–14.

199. Schnell S, Rose MJ, Wu C, Garcia J, Robinson JD, Markl M, Rigsby CK. Improved assessment of aortic hemodynamics by k-t accelerated dual-venc 4D flow MRI in pediatric patients. J Cardiovasc Magn Reson. 2016;18:O96.

200. Lee AT, Pike GB, Pelc NJ. Three-point phase-contrast velocity measurements with increased velocity-to-noise ratio. Magn Reson Med. 1995;33:122–6.

201. Pipe JG. A simple measure of flow disorder and wall shear stress in phase contrast MRI. Magn Reson Med. 2003;49:543–50.

202. Binter C, Knobloch V, Manka R, Sigfridsson A, Kozerke S. Bayesian multipoint velocity encoding for concurrent flow and turbulence mapping. Magn Reson Med. 2013;69:1337–45.

203. Loecher M, Ennis DB. Velocity reconstruction with nonconvex optimization for low-velocity-encoding phase-contrast MRI. Magn Reson Med. 2018;80:42–52.

204. Bustamante M, Petersson S, Eriksson J, Alehagen U, Dyverfeldt P, Carlhäll C-J, Ebbers T. Atlas-based analysis of 4D flow CMR: automated vessel segmentation and flow quantification. J Cardiovasc Magn Reson. 2015;17:87.

205. Schrauben E, Wåhlin A, Ambarki K, Spaak E, Malm J, Wieben O, Eklund A. Fast 4D flow MRI intracranial segmentation and quantification in tortuous arteries. J Magn Reson Imaging. 2015;42:1458–64.